The monitoring nitrous oxide sources (MIN2OS) satellite project

Philippe Ricaud, Jean-Luc Attié, Rémi Chalinel, Frédérick Pasternak, Joël Léonard, Isabelle Pison, Elizabeth Pattey, Rona L. Thompson, Zdenek Zelinger, Jos Lelieveld, et al.

Remote Sensing of Environment 266 (2021) 112688

Contents lists available at ScienceDirect

Remote Sensing of Environment

journal homepage: www.elsevier.com/locate/rse

The Monitoring Nitrous Oxide Sources (MIN_2OS) satellite project

Philippe Ricaud [a,*], Jean-Luc Attié [b], Rémi Chalinel [b], Frédérick Pasternak [c], Joël Léonard [d], Isabelle Pison [e], Elizabeth Pattey [f], Rona L. Thompson [g], Zdenek Zelinger [h], Jos Lelieveld [i], Jean Sciare [j], Naoko Saitoh [k], Juying Warner [l], Audrey Fortems-Cheiney [e], Hélène Reynal [m], Jérôme Vidot [a], Laure Brooker [c], Laurent Berdeu [c], Olivier Saint-Pé [c], Prabir K. Patra [n], Michal Dostál [h], Jan Suchánek [h], Václav Nevrlý [h], Christine Groot Zwaaftink [g]

[a] CNRM, Université de Toulouse, Météo-France, CNRS, Toulouse, France
[b] Laboratoire d'Aérologie, Université de Toulouse, CNRS, UPS, Toulouse, France
[c] AIRBUS Defence and Space, Toulouse, France
[d] INRAE, Barenton-Bugny, France
[e] Laboratoire des Sciences du Climat et de l'Environnement, LSCE-IPSL (CEA-CNRS-UVSQ), Université Paris-Saclay, 91191 Gif-sur-Yvette, France
[f] AAFC, Ottawa, ON, Canada
[g] NILU – Norsk Institutt for Luftforskning, Kjeller, Norway
[h] JHIPC, Prague, Czech Republic
[i] MPIC, Mainz, Germany
[j] Cyprus Institute, Nicosia, Cyprus
[k] Chiba University, Chiba, Japan
[l] Maryland University, USA
[m] INRAE, Castanet-Tolosan, France
[n] Research Institute for Global Change, JAMSTEC, Yokohama, 236-0001, Japan

ARTICLE INFO

Edited by: Menghua Wang

ABSTRACT

The Monitoring Nitrous Oxide Sources (MIN_2OS) satellite project aims at monitoring global-scale nitrous oxide (N_2O) sources by retrieving N_2O surface fluxes from the inversion of space-borne N_2O measurements that are

Abbreviations: 4D-Var, 4D-variational; AGAGE, Advanced Global Atmospheric Gases Experiment; AIRS, Atmospheric InfraRed Sounder; ANR, Agence Nationale de la Recherche; AOD, Aerosol Optical Depth; ATOM, Atmospheric Tomography Mission; BT, Brightness Temperature; BU, Bottom Up; CAMS, Copernicus Atmosphere Monitoring Service; CIF, Community Inversion Framework; CTM, Chemical Transport Model; DayCent, Daily Century; DNDC, DeNitrification-DeComposition; DOF, Degree-of-Freedom; ECMWF, European Centre for Medium-Range Weather Forecasts; EDGAR, Emissions Database for Global Atmospheric Research; EE11, Earth Explorer 11; ERA5, ECMWF Reanalyses v5; ESA, European Space Agency; EUMETSAT, European Organisation for the Exploitation of Meteorological Satellites; FLEXPART, FLEXible PARTicle dispersion model; FTIR, Fourier-transform infrared spectroscopy; FWHM, Full Width at Half Maximum; GAW/WMO, Global Atmosphere Watch/World Meteorological Organisation; GHG, Greenhouse gas; GOSAT, Greenhouse gases Observing SATellite; GOSAT-2, Greenhouse gases Observing SATellite-2; HIPPO, HIAPER Pole-to-Pole Observations; HRES, High RESolution; IASI, Infrared Atmospheric Sounding Interferometer; IASI-NG, Infrared Atmospheric Sounding Interferometer-New Generation; ICOS, Integrated Carbon Observation System; IPCC, Intergovernmental Panel on Climate Change; LBLRTM, Line-By-Line Radiative Transfer Model; LEO, Low Earth Orbit; LMDz, Laboratoire de Météorologie Dynamique; LT, Local Time; LWIR, LongWave InfraRed; MACSUR, Modelling European Agriculture with Climate Change for Food Security; Metop-SG, Metop-Second Generation; MIN_2OS, Monitoring Nitrous Oxide Sources; MIROC-4, Model for Interdisciplinary Research on Climate – version 4; MWIR, MidWave InfraRed; NASA, National Aeronautics and Space Administration; NDACC, Network for the Detection of Atmospheric Composition Change; NEdR, Noise Equivalent delta Radiance; NEdT, Noise Equivalent differential Temperature; NLTE, Non-Local Thermodynamic Effect; NOAA, National Oceanic and Atmospheric Administration; RTTOV, Radiative Transfer for Tiros Operational Vertical sounder; Sentinel-2 NG, Sentinel-2 New Generation; SNR, Signal-to-Noise Ratio; STICS, Simulateur mulTIdisciplinaire pour les Cultures Standard; TCCON, Total Carbon Column Observing Network; TD, Top Down; TIR, Thermal InfraRed; TN_2OR, Toulouse N_2O Retrieval; TRL, Technology Readiness Level; UNFCCG, United Nations Framework Convention on Climate Change; VMR, Volume Mixing Ratio.

* Corresponding author.
E-mail addresses: philippe.ricaud@meteo.fr (P. Ricaud), jean-luc.attie@aero.obs-mip.fr (J.-L. Attié), remi.chalinel@aero.obs-mip.fr (R. Chalinel), frederick.pasternak@airbus.com (F. Pasternak), joel.leonard@inra.fr (J. Léonard), isabelle.pison@lsce.ipsl.fr (I. Pison), elizabeth.pattey@agr.gc.ca (E. Pattey), rlt@nilu.no (R.L. Thompson), zdenek.zelinger@jh-inst.cas.cz (Z. Zelinger), jos.lelieveld@mpic.de (J. Lelieveld), j.sciare@cyi.ac.cy (J. Sciare), nsaitoh@faculty.chiba-u.jp (N. Saitoh), audrey.fortems@lsce.ipsl.fr (A. Fortems-Cheiney), helene.raynal@inrae.fr (H. Reynal), jerome.vidot@meteo.fr (J. Vidot), laure.brooker@airbus.com (L. Brooker), laurent.berdeu@airbus.com (L. Berdeu), olivier.saintpe@airbus.com (O. Saint-Pé), prabir@jamstec.go.jp (P.K. Patra), michal.dostal@jh-inst.cas.cz (M. Dostál), jan.suchanek@jh-inst.cas.cz (J. Suchánek), cgz@nilu.no (C.G. Zwaaftink).

https://doi.org/10.1016/j.rse.2021.112688
Received 28 April 2021; Received in revised form 2 August 2021; Accepted 2 September 2021
Available online 16 September 2021

Keywords:
Nitrous oxide
N_2O emissions
Space-borne observations
Sources
Modelling

sensitive to the lowermost atmospheric layers under favorable conditions. MIN$_2$OS will provide emission estimates of N_2O at a horizontal resolution of $1^\circ \times 1^\circ$ on the global scale and 10×10 km^2 on the regional scale on a weekly to monthly basis depending on the application (e.g., agriculture, national inventories, policy, scientific research). Our novel approach is based on the development of: 1) a space-borne instrument operating in the Thermal InfraRed domain providing, in clear sky conditions, N_2O mixing ratio in the lowermost atmosphere (900 hPa) under favorable conditions (summer daytime) over land and under favorable and unfavorable (winter nighttime) conditions over the ocean and 2) an atmospheric inversion framework to estimate N_2O surface fluxes from the atmospheric satellite observations. After studying three N_2O spectral bands (B1 at 1240–1350 cm^{-1}, B2 at 2150–2260 cm^{-1} and B3 at 2400–2600 cm^{-1}), a new TIR instrument will be developed, centered at 1250–1330 cm^{-1}, with a resolution of 0.125 cm^{-1}, a Full Width at Half Maximum of 0.25 cm^{-1} and a swath of 300 km. To optimally constrain the retrieval of N_2O vertical profiles, the instrument will be on-board a platform at ~830 km altitude in a sun-synchronous orbit crossing the Equator in descending node at 09:30 local time in synergy with two other platforms (Metop-SG and Sentinel-2 NG) expected to fly in 2031–32 aiming at detecting surface properties, agricultural information on the field scale and vertical profiles of atmospheric constituents and temperature. The lifetime of the MIN$_2$OS project would be 4–5 years to study the interannual variability of N_2O surface fluxes. The spectral noise can be decreased by at least a factor of 5 compared to the lowest noise accessible to date with the Infrared Atmospheric Sounding Interferometer-New Generation (IASI-NG) mission. The N_2O total error is expected to be less than ~1% (~3 ppbv) along the vertical. The preliminary design of the MIN$_2$OS project results in a small instrument (payload of 90 kg, volume of $1200 \times 600 \times 300$ mm^3) with, in addition to the spectrometer, a wide field and 1-km resolution imager for cloud detection. The instruments could be hosted on a small platform, the whole satellite being largely compatible with a dual launch on VEGA-C. The MIN$_2$OS project has been submitted to the European Space Agency Earth Explorer 11 mission ideas.

1. Introduction

Nitrous oxide (N_2O) is the third most important long-lived greenhouse gas (GHG) after carbon dioxide (CO_2) and methane (CH_4) contributing to global warming. It has a global warming potential 298 times higher than that of CO_2 on a mass basis and for a 100-year horizon (IPCC, 2007). Consequently, N_2O has a radiative forcing of climate 10% that of CO_2, although it is 1000 times less abundant over the time period from 1750 to present. Furthermore, emissions of N_2O are currently the most important emissions of any stratospheric ozone depleting substance and are impeding the recovery of the ozone hole (Ravishankara et al., 2009). N_2O emissions increased by 0.25–0.30% yr^{-1} over the past 10 years (Tian et al., 2020) and keep increasing until 2100 (IPCC, 2007) in the majority of socio-economic scenarios.

Emissions of N_2O are largely driven by the microbial processes of nitrification and denitrification occurring in soils, the ocean and freshwater systems (Bakker et al., 2014). In addition, there is a smaller source of abiotic emissions through incomplete combustion and some industrial processes (Davidson and Kanter, 2014). Of the global total emission (~17 TgN yr^{-1}), ~57% is naturally occurring and the remaining ~43% is anthropogenic (Tian et al., 2020). Anthropogenic emissions are dominated by agriculture (~52%) and are due to the perturbation of the nitrogen cycle through the addition of nitrogen from synthetic fertilizers and manure, while industrial and fossil fuel combustion contributes ~27% (Tian et al., 2020). Once emitted into the atmosphere, N_2O remains there for an average of ~116 years (Prather et al., 2015), while it is removed in the stratosphere via photodissociation and oxidation by the oxygen radical O(^{1}D). This is also the main pathway of stratospheric nitrogen oxide production involved in ozone (O_3) depletion (Minschwaner et al., 1993).

Since N_2O emissions (natural and anthropogenic) are predominantly driven by microbial processes, which depend strongly on the environmental conditions (soil water content, temperature, oxygen availability, etc.) and management practices, the emissions are extremely challenging to simulate and forecast. Emission inventories, as reported to the United Nations Framework Convention on Climate Change (UNFCCC), are based on the Intergovernmental Panel on Climate Change (IPCC) Tier-1 and Tier-2 emission factor approaches (IPCC, 2007, 2019), which combine emission factors for different source sectors (e.g., direct emissions from agriculture) with activity data. However, the uncertainty in emission factors is up to 300%, representing a major uncertainty in the total GHG emissions (in CO_2 equivalents) from agriculture and waste sectors (De Klein et al., 2006). Moreover, the impact of varying environmental conditions on the emissions is not captured in the inventories (Tian et al., 2015; Ehrhardt et al., 2017). Asides from the IPCC approach, N_2O emissions from land and ocean can be either estimated by process-based ecosystem models (a bottom-up (BU) approach) or based on changes in atmospheric N_2O mixing ratio with the help of an atmospheric chemistry-transport model (a top-down (TD) approach). Based on BU approaches (Tian et al., 2020), the overall N_2O emission estimates exhibit a large range, from 12.2 to 23.5 Tg N yr^{-1}, with natural emissions ranging from 8.0 to 12.0 Tg N yr^{-1}, including natural soils (4.9–6.5 Tg N yr^{-1}) and ocean (2.5–4.3 Tg N yr^{-1}), and anthropogenic emissions ranging from 4.2 to 11.4 Tg N yr^{-1}. A large divergence exists in the estimation of natural soil N_2O emission by inventories, empirical and process-based models, implying that our understanding of the processes and their controls remains uncertain. This also leads to considerable uncertainty in the trend in N_2O emission over the recent decades. The latest estimate of the global N_2O emission trend from 1998 to 2016 is 0.8 ± 0.2 Tg N yr^{-1} per decade using BU modelling. More generally, the uncertainties in the BU estimates arise from the difficulty of modelling the complex non-linear processes leading to N_2O production and consumption on land and in the ocean.

The N_2O surface emissions show huge temporal and spatial variabilities. The spatial variability on the global scale is estimated to be greater than a factor 10 over land (Tian et al., 2020) and greater than a factor 5 over the ocean (Nevison et al., 1995). For anthropogenic emissions, East and South Asia, Europe and North America are the most emitting regions, while for natural soil emissions, Equatorial and South Africa and South America are the most emitting regions. For the ocean, the Eastern Equatorial Pacific, South-Eastern tropical Atlantic and Eastern Indian Oceans are the main N_2O source areas. On the local/regional scale, in situ flux measurements show that the diurnal variability of the N_2O flux over a cultivated plot is $\pm$20% (Alves et al., 2012; Shurpali et al., 2016). Over a region/territory in France, the spatial variability as calculated by the Simulateur mulTIdisciplinaire pour les Cultures Standard (STICS) model is greater than a factor 6 (Therond et al., 2017). Even in one location, N_2O emissions vary depending on the management practices and weather conditions. Emission peaks usually follow nitrogen fertilizer application (e.g., Grant and Pattey, 2003; Metivier et al., 2009) driven by rainfall or irrigation. For soil freezing regions, they follow snowmelt and soil thawing (e.g., Grant and Pattey, 1999; Pattey et al., 2007, 2008; Wagner-Riddle et al., 2017).

Given the large spatiotemporal variability in N_2O emissions, and the challenges to simulate the processes driving the emissions, it is essential to have reliable and accurate estimates also from TD approaches. Up to

now, TD estimates of N_2O emissions relied on sparse surface observations (e.g., international networks of observation sites, complemented with aircraft (e.g., Desjardins et al., 2010) and ship campaign measurements) to derive monthly sources and sinks of N_2O on the global (e.g., Thompson et al., 2014) and European scales (e.g., Bergamaschi et al., 2015). These estimates are based on the atmospheric inversion approach, which uses Bayesian statistics and atmospheric chemistry-transport models to relate the changes in atmospheric concentrations to changes in surface-atmosphere fluxes.

On the global scale, BU and TD estimates of the N_2O emission trend from 1998 to 2016 are in good agreement: 0.8 ± 0.2 Tg N yr^{-1} per decade for BU modelling, compared to 1.1 ± 0.6 Tg N yr^{-1} per decade using atmospheric inversions (Tian et al., 2020). Nevertheless, recent TD estimations of the emission increase since 2009 were twice as large as those predicted by the IPCC emission factor approach (Thompson et al., 2019). To understand and decrease these discrepancies, much more work on the estimation of regional N_2O emissions is needed. In particular, tropical and sub-tropical areas, in addition to being important source regions, are also domains where the largest uncertainties and discrepancies between TD and BU approaches exist. One major problem in the tropics and sub-tropics for TD approaches is the very sparse atmospheric N_2O observation network (Wells et al., 2018; Thompson et al., 2014). More observations over these regions would help resolve key questions, such as: i) the impact of climate variability on tropical rainforest emissions, e.g., the standard deviation of annual emissions has been reported to be up to 100% over a 10-year period (Werner et al., 2007) and ii) the impact of land-use changes on emissions, e.g., drainage of wetland/peatland, deforestation, and conversion of cleared land for agriculture. There are also open issues concerning N_2O emission from some emerging technologies. Ammonia (NH_3) is proposed as a viable carbon-free energy carrier for transportation and power generation (e.g., Kurata et al., 2017). Combustion of NH_3 (pure or mixed with other fuels, e.g., CH_4) could be a potentially significant source of reactive nitrogen species (NO_x = NO+NO_2 and NH_3) as well as N_2O (through incomplete combustion) in the future. However, there are too few studies examining the chemical reactions of NH_3 combustion in order to make reliable predictions of NO_x and N_2O emissions.

Satellite data are thought to be a potential source of information for TD approaches, able to complement the sparse in-situ measurements, particularly in key regions which are remote and difficult to access, such as tropical areas. Since 2008, Thermal InfraRed (TIR) measurements from satellite instruments such as the Infrared Atmospheric Sounding Interferometer (IASI), Atmospheric InfraRed Sounder (AIRS), and Greenhouse Gases Observing Satellite (GOSAT) have become available to observe the N_2O total column and upper tropospheric N_2O. In the TIR domain, on average, the vertical sensitivity of the N_2O retrievals, as defined by the averaging kernels, in which the maximum is mainly in the upper troposphere around 300 hPa for all the current sensors, AIRS (Xiong et al., 2014), GOSAT (Kangah et al., 2017) and IASI (Chalinel et al., 2021, paper in this special issue).

Initial studies have shown that it is possible to follow long-range transport via the temporal and spatial variability of N_2O total column. In the tropics, the convergences of the Walker cells from the American continent and the Indian Ocean to the African continent produced a local maximum over Africa in the IASI N_2O total columns officially processed by the European Organisation for the Exploitation of Meteorological Satellites (EUMETSAT; Ricaud et al., 2009). In the extra-tropics over the Mediterranean Basin, the summertime maximum of upper tropospheric N_2O observed by GOSAT in the East compared to the West (Kangah et al., 2017; Ricaud et al., 2014) has been attributed to the impact of the Asian monsoon anticyclone, which redistributes the elevated N_2O concentration in the lower troposphere of the Indian subcontinent and Eastern China by uplift to the upper troposphere where it is transported towards Northern Africa and the Mediterranean Basin (Ricaud et al., 2014).

Climatological studies (with monthly to yearly averages) similar to those using horizontal bins of 2° × 2° with GOSAT data can now be achieved on the global scale in the upper troposphere over 1 day and at a horizontal resolution of 1° × 1° (about 100 × 100 km^2) by using the measurements from IASI (Chalinel et al., 2021). Upper tropospheric N_2O from IASI is retrieved using the TN_2OR (Toulouse N_2O Retrieval) V1.7 tool combining the Radiative Transfer for Tiros Operational Vertical sounder (RTTOV) model version v11.2 (Saunders et al., 1999) and the Levenberg-Marquardt method (Levenberg, 1944; Marquardt, 1963), a non-linear inversion algorithm based on the optimal estimation method (Rodgers, 2000). Simultaneous retrievals of N_2O, CH_4, water vapor (H_2O), temperature and surface temperature and emissivity are performed considering the TIR band 1240–1350 cm^{-1} and produce vertical profiles of N_2O with a total error better than 1%.

Until now, quantifying N_2O emissions by TD approaches relied on sparse surface observations to derive monthly sources of N_2O on the global scale. Nowadays, N_2O space-borne observations are mainly performed in the TIR domain and are mainly sensitive in the upper troposphere (around 300 hPa), which explains why they are not yet assimilated in TD approaches targeting surface fluxes. The Monitoring Nitrous Oxide Sources (MIN_2OS) satellite project, submitted to the European Space Agency (ESA) Earth Explorer 11 (EE11) mission ideas, has been set up to provide N_2O sources at high temporal and horizontal resolutions on the global scale. Our novel approach is based on the development of: 1) a space-borne instrument operating in the TIR domain inherited from a more sensitive version of the IASI and IASI-NG instruments, providing N_2O mixing ratio in the lowermost troposphere (900 hPa) under favorable conditions (summer daytime) over land and all conditions over the ocean and 2) an inversion source model to estimate, from atmospheric satellite observations, N_2O surface fluxes.

To fulfill the MIN_2OS objectives, we propose a new TIR instrument. Our objective is to describe our theoretical studies to better determine the TIR instrument specifications and its deployment on a platform to better monitor N_2O mixing ratio in the lowermost troposphere. In Section 2, we first present the MIN_2OS project. We then describe in Section 3 the MIN_2OS instrumental concept through the development of a scientific tool that will help to identify the best configuration (spectral band and resolution, retrieval parameters, vertical sensitivity, etc.) associated with the instrument specifications (spectral noise achievable, spectral resolution, etc.) and the platform (orbit altitude, swath, etc.). The MIN_2OS system solution presenting the actual devices selected for the project are explained in Section 4. Section 5 presents the MIN_2OS mission including the instrument and the platform definition. Preliminary studies on the potential impact of MIN_2OS observations on retrieving N_2O surface fluxes are presented in Section 6 on the global and regional scales before concluding in Section 7.

2. The MIN_2OS project

2.1. The concept

There are currently no satellite observations sensitive to N_2O in the lower troposphere and with sufficient precision and accuracy to be used to determine surface-atmosphere fluxes. Such measurements are more pertinent than ever to reduce uncertainties in the emissions and to monitor the evolution of this important GHG, which will very likely continue to increase in the future. The MIN_2OS project intends to:

1) provide satellite measurements with a high sensitivity near the surface and unprecedented precision,
2) develop a Bayesian flux inversion tool based on a 4D-variational (4D-Var) assimilation method using state-of-the-art atmospheric chemistry transport models (at least one regional and one global model will be used),
3) use process-based modelling to estimate N_2O surface fluxes on the local scale and aggregate them on the regional scale,

4) validate the inversion-based flux estimates against independent data (measurements and modelling),
5) distribute N_2O flux data to external users (scientists, policy-makers, and other stakeholders).

Because today's TIR space-borne instruments (i.e., IASI, GOSAT and AIRS) mainly provide N_2O measurements with a high sensitivity in the upper troposphere, our objective is to develop a new instrument, detailed in Section 3, that will provide three independent vertical atmospheric layers of N_2O measurements in the lowermost, in the middle and in the upper troposphere (i.e., 900, 600 and 300 hPa, respectively). The vertical sensitivity is important for the inversion of sources/sinks because the N_2O mixing ratios (total column or in the upper troposphere and stratosphere altitudes) are strongly affected by photochemical loss in the stratosphere (Saito et al., 2012). The MIN$_2$OS instrument, based on the heritage of IASI and IASI-NG, will have a much higher signal-to-noise ratio, (i.e., 3–5 times higher than the one of IASI-NG). It will operate in the TIR, on the N_2O absorption band in the spectral domain of 1240–1320 cm^{-1}, with a resolution of 0.125 cm^{-1}, a Full Width at Half Maximum (FWHM) of 0.25 cm^{-1} and a swath of 300 km (±150 km). In a sun-synchronous orbit at around 830 km altitude, the platform should fly with other platforms expected to fly in 2031 (e.g., Metop-SG equipped with IASI-NG, Sentinel-2 NG) in order to have access to coincident meteorological and chemical information such as temperature, humidity, clouds, and aerosols that will be used to analyze the MIN$_2$OS radiances.

The main advantage of the MIN$_2$OS instrument is to provide N_2O information in the lowermost troposphere, namely as close as possible to the source location. A good sensitivity in a vertical layer as close as possible to the surface will help to minimize errors due to the transport of air masses from the measurement location back to the source when applying the 4D-Var assimilation system to invert the surface N_2O sources (see Section 6). However, in some circumstances (e.g., presence of clouds, deep convection), the enriched-N_2O air masses detected by the MIN$_2$OS instrument might be far from the source and/or in the upper troposphere as during the summertime Asian monsoon studied in Kangah et al. (2017) with GOSAT observations. In such cases, the MIN$_2$OS instrument will be able to track these N_2O-enriched air masses due to its sensitivity within the lowermost, middle and upper troposphere. We recall that the aim of the source inversion is not to track air masses but to retrieve information on the emissions, to which the observed concentrations are sensitive. This is why the time resolution of the optimized fluxes can be coarse in time (from a week to a month) relative to the modelling of atmospheric transport. Therefore, it is not necessary to resolve daily (or higher frequency) fluxes, which are also of less relevance for policy-makers and main stakeholders. Nevertheless, data would be available almost every day of the whole month and will help better constrain the monthly (or weekly) mean fluxes.

The aim of the MIN$_2$OS technical concept is to develop a TIR instrument to obtain good quality N_2O vertical profiles in the lowermost layers of the troposphere and then systematically produce profiles on the global scale at a horizontal resolution of $1^\circ \times 1^\circ$ and on the regional scale at a horizontal resolution of 10×10 km^2. The temporal evolution of N_2O depends on several factors such as the timing and rates of nitrogen-based fertilizer application, meteorology (rainfall, snowmelt), soil texture, soil water saturation, and crop. A diurnal cycle in the N_2O surface flux has been observed with a maximum around 12:00–14:00 local time (LT) and a minimum around 08:00 LT (Charteris et al., 2020). As a consequence, sampling between 09:00 and 10:00 LT was recommended to capture the daily mean N_2O flux in temperate climates (Alves et al., 2012) that is consistent with the fact that MIN$_2$OS will fly in convoy with Metop-SG equipped with IASI-NG and Sentinel-2 NG with a time of Equator crossing to about 09:30 LT. There is also a stringent constraint to obtain N_2O measurements in the lowermost troposphere at very high horizontal resolution. Consequently, the favored approach is to take advantage of the heritage of IASI and IASI-NG to specify an instrument with a much higher signal to noise ratio than the ones of both IASI and IASI-NG, given that the temporal sampling will be imposed by the platform flying in convoy with the MIN$_2$OS platform. In the two following subsections, we present the spectral and vertical sensitivities of the present-day (IASI) and the future (IASI-NG) instruments to obtain N_2O information along the vertical, together with a new instrument that has the same spectral resolution as IASI-NG but a signal-to-noise ratio increased by a factor 3 or 5 compared to IASI-NG.

2.2. Spectral sensitivity

We first need to evaluate how the N_2O retrievals obtained with IASI-NG might be affected by the two following technical improvements: spectral resolution and signal-to-noise ratio compared to the N_2O retrievals obtained with IASI (see Chalinel et al., 2021). To do so, we used the Radiative Transfer for TIROS Operational Vertical sounder (RTTOV) model (Saunders et al., 1999) coupled with the Optimal Estimation method (Rodgers, 2000) in a way consistent with the analyses presented in Chalinel et al. (2021). For our retrieval system, we used RTTOV version 12.0 together with the regression coefficients v9 based on the model LBLRTM (LBL Radiative Transfer Model) (Hocking et al., 2015). In this version, the 25 predictors depend on the trace gas profiles including H_2O, O_3, CO_2, N_2O, CH_4 and carbon monoxide (CO).

Previous studies (e.g., Clerbaux et al., 2009) have highlighted 3 absorption bands of N_2O in the IASI spectral range centered at ~1280 cm^{-1} (7.8 μm), ~2220 cm^{-1} (4.5 μm) and ~2550 cm^{-1} (3.9 μm). Fig. 1 shows a N_2O weighting function matrix (Jacobian matrix) calculated in units of brightness temperature (BT) for the IASI instrument for one pixel selected over France in favorable conditions (summer daytime) and presented in Table 2 and Fig. 3. This matrix represents the sensitivity of the calculated BT to a unit change in the N_2O volume mixing ratio (vmr). Note that the N_2O Jacobian matrices associated to the 2×15 pixels selected in favorable and unfavorable conditions (see Table 2 and Fig. 3) are shown in the Supplementary Material in Figs. S1 and S2, respectively. The spectral signature of N_2O appears in the three spectral regions with significant differences of intensity. The most intense absorption band is between 2190 and 2240 cm^{-1} (4.5 μm) and shows sensitivity to N_2O from the lowermost troposphere to 100 hPa with a maximum of sensitivity between 500 and 200 hPa. The absorption band located between 1250 and 1310 cm^{-1} (7.8 μm) is less intense than the previous band and is sensitive to N_2O between 1000 and 100 hPa. The third band located between 2500 and 2600 cm^{-1} (7.8 μm) is much less intense than the two other bands and is sensitive to N_2O from 900 to 300 hPa.

To illustrate the sensitivity of these 3 bands to N_2O and to the other atmospheric and surface parameters, a sensitivity study (Fig. 2) has been performed using a set of atmospheric and surface parameters representative of a given atmospheric state consistent with, as an example, one pixel over France in summer daytime (see Table 2 and Fig. 3). Note that the spectral sensitivity associated to the 2×15 pixels selected in favorable and unfavorable conditions (see Table 2 and Fig. 3) are shown in the Supplementary Material in Figs. S3 and S4, respectively. This study consists in calculating the variation of the absolute value of BT (called hereafter $|\Delta BT|$) over the IASI-NG spectral range and resolution (consistent with MIN$_2$OS) for a 1% variation of the major atmospheric constituents and surface emissivity and 1 K variation of temperature profiles and surface. We selected the 3 following bands as follow: B1 (1240–1350 cm^{-1}), B2 (2150–2260 cm^{-1}) and B3 (2400–2500 cm^{-1}). The band B1 is mainly sensitive to: H_2O, temperature, CH_4, surface temperature and surface emissivity. The band B2 is mainly sensitive to: H_2O, temperature, CO_2, CO and O_3, surface temperature and surface emissivity. The band B3 is mainly sensitive to: H_2O, temperature, surface temperature and surface emissivity.

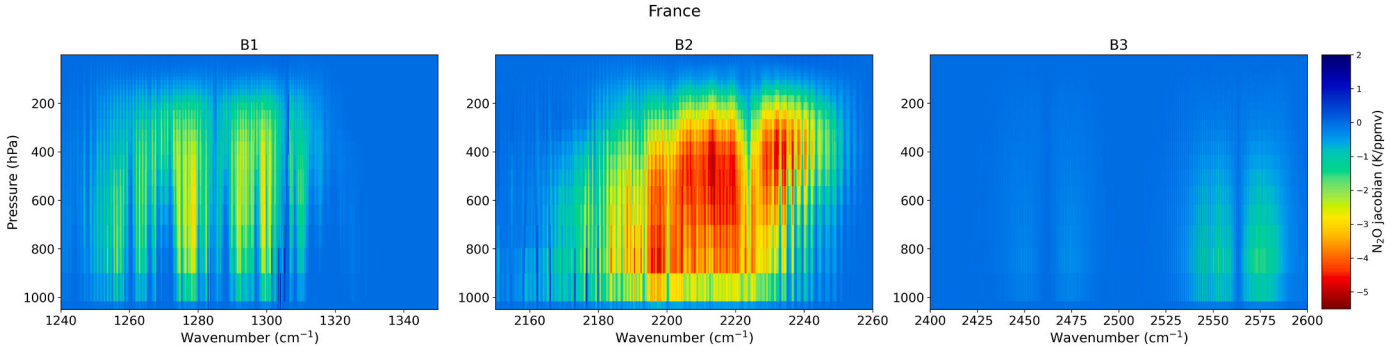

Fig. 1. N_2O Jacobian in brightness temperature (K/ppmv) calculated by RTTOV for one pixel selected over France in favorable conditions (summer daytime) and presented in Table 2 and Fig. 3, over the 3 IASI spectral micro-windows of 1240–1350 cm^{-1} (B1, left), 2150–2260 cm^{-1} (B2, middle), and 2400–2600 cm^{-1} (B3, right). Note the colour scale is logarithmic.

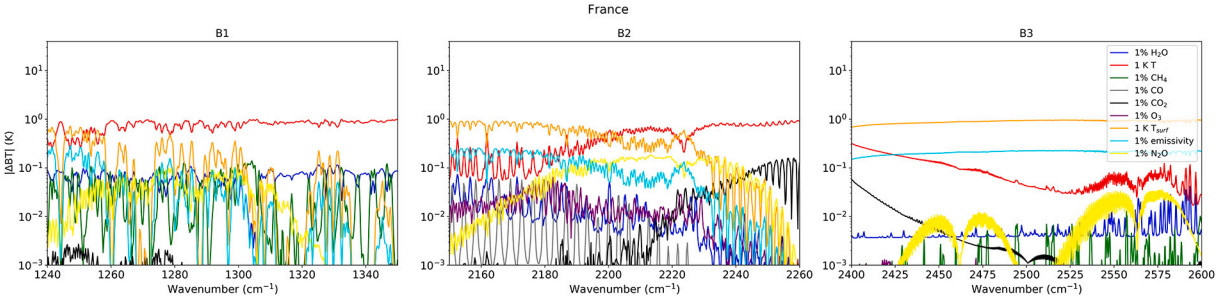

Fig. 2. Absolute change in brightness temperature ($|\Delta BT|$) for one pixel selected over France in favorable conditions (summer daytime) and presented in Table 2 and Fig. 3 for 1% change in: H_2O (dark blue), CH_4 (green), CO (grey), CO_2 (black), O_3 (purple), N_2O (yellow), and surface emissivity (light blue) and for 1 K change in: temperature profile (red), and surface temperature (orange) for the IASI-NG (consistent with MIN$_2$OS spectral resolution) over France in summer daytime in B1, B2 and B3. The y axis is in logarithmic scale. (For interpretation of the references to colour in this figure legend, the reader is referred to the web version of this article.)

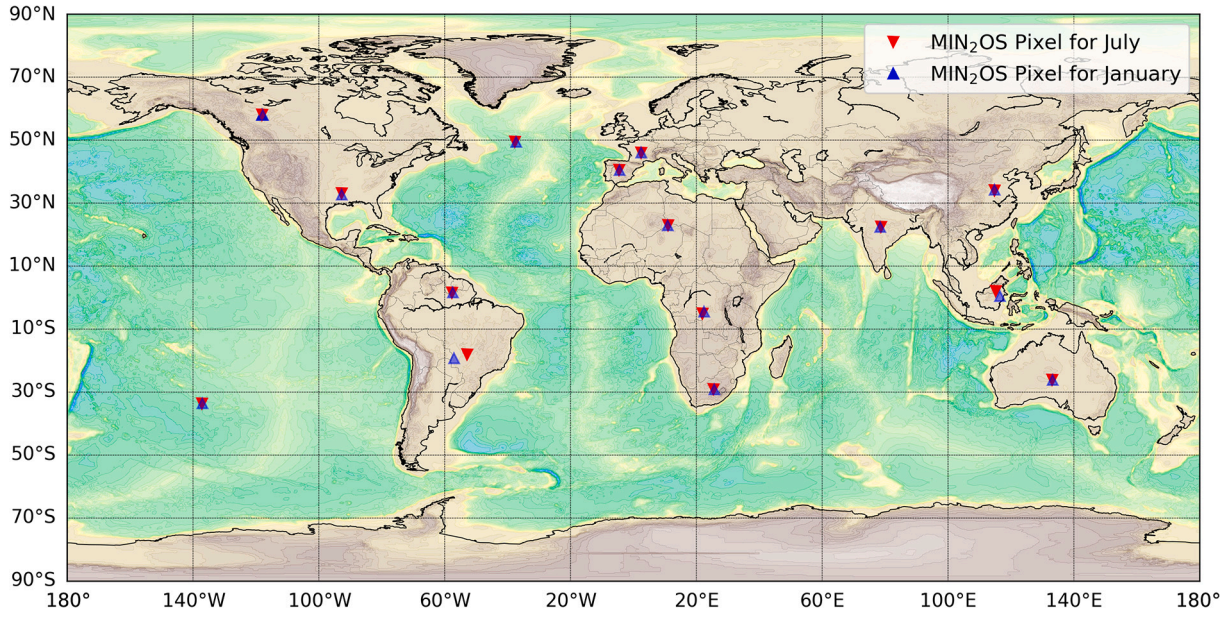

Fig. 3. Locations of the 2 × 15 MIN$_2$OS pixels (red triangles for July 2011 and blue triangles for January 2011 – dates and times of observations are listed in Table 2) used to highlight the radiance residuals, the averaging kernels, the DOFs, the N_2O total errors and the N_2O error contaminations. (For interpretation of the references to colour in this figure legend, the reader is referred to the web version of this article.)

2.3. Vertical sensitivity

To evaluate the retrievals of N_2O profiles considering different configurations of the MIN$_2$OS instruments, we have used and adapted the TN$_2$OR V1.7 tool initially developed to analyze IASI spectral measurements (Chalinel et al., 2021). The restitution process goes through several steps and uses mainly the RTTOV model version 12 and the Levenberg-Marquardt method that is a non-linear inversion algorithm

based on the optimal estimation method. For MIN_2OS, the IASI-NG instrumental line shape has been selected in RTTOV, providing a spectral resolution of 0.125 cm^{-1}, and a FWHM of 0.25 cm^{-1}. Depending on the band studied (B1 to B3), we used the a priori information and errors in the a priori covariance matrices consistent with Table 1. These values were consistent with the IASI study presented in Chalinel et al. (2021). We have to note that the expected improvement of the IASI-NG accuracy compared to the IASI accuracy on the retrievals of several species has been presented in Crevoisier et al. (2014): 0.1 to 0.5% for tropospheric temperature, 0–8% for tropospheric H_2O, 5–47% for CH_4 tropospheric columns, 5–5% for CO_2 tropospheric columns, and 3–51% for tropospheric O_3. This means that the configuration of our retrieval a priori and error covariance matrices for MIN_2OS can be considered as pessimistic and could be improved in the future.

The total error was evaluated as the sum of the smoothing error (issued from the covariance matrix of the a priori state) and the measurement error (issued from the error covariance matrix of the observed spectral radiance). In band B1, we have selected the variables to be retrieved to be: N_2O, CH_4, H_2O, temperature (T), surface temperature (T_s) and surface emissivity (ε). In band B2, the variables to be retrieved are: N_2O, H_2O, O_3, CO_2, CO, T, T_s and ε. And, in band B3, the variables to be retrieved are: N_2O, H_2O, T, T_s and ε. Note that ocean emissivity models are very accurate but we can expect more errors over land surfaces due to unknowns about viewing-angle dependence of some surface types such as desert. A value of 1% over ocean is attainable but, above land surfaces, values ranging 2–5% can be expected (Loveless et al., 2021), namely still less that the a priori error on surface emissivity (Δε) fixed to be 15% in our study.

For each band, the Signal-to-Noise Ratio (SNR) associated with MIN_2OS was tuned to be either three times or five times higher than the one associated with IASI-NG. Consistent with the study presented in Chalinel et al. (2021), the retrieval process was applied for the 2 × 15 pixels presented in Fig. 3 and Table 2, which correspond to 2 extreme conditions in the TIR domain caused by the impact of the thermal contrast on the vertical sensitivity of the observations, namely in favorable (summer daytime) and unfavorable (winter nighttime) conditions over land and the ocean.

Concretely, to determine for the MIN_2OS project the spectral and vertical sensitivities, total random errors and contaminations, we have used spectral radiances measured by IASI over 0.5 cm^{-1} resolution in the bands B1, B2 and B3 in the vicinity of 15 sites in favorable and unfavorable conditions. This set of 30 radiances is then spectrally interpolated into 0.25 cm^{-1} to reach the IASI-NG and MIN_2OS spectral resolutions. The noise associated to the 3 bands is then: 1) the IASI noise, 2) the IASI-NG noise, and 3) the MIN_2OS noise that is to say the IASI-NG noise divided either by 3 or by 5. The TN_2OR V1.7 tool is then applied to the 2 × 15 spectral radiances consistent with IASI, IASI-NG or MIN_2OS (SNR × 3 or 5 compared to the one of IASI-NG) to obtain vertical profiles and associated random errors of a set of geophysical variables including N_2O. Three points are worthwhile mentioning. 1) The Optimal Estimation Method is an unbiased random retrieval method. As a consequence, we have not calculated systematic errors but we have estimated the contamination factor (Chalinel et al., 2021) on the N_2O estimation induced by the parameters simultaneously retrieved (see Section 3.4). 2) The retrieved radiances are debiased against the observed radiances, this has the main advantage of lessening the impact of systematic errors (such as the spectroscopic errors) on the retrieved species. From Matricardi (2009), the differences between radiances observed by IASI and radiances calculated by RTTOV in the MIN_2OS bands B1, B2 and B are ranging −0.8 to 0.0 K, −1.2 to 0.0 K and − 0.8 to 0.1 K, respectively in the Northern Hemisphere, −1.6 to 0.4 K, −1.2 to 1.2 K and − 1.0 to −0.4 K, respectively in the tropics, and − 0.8 K to 0.2 K, −1.2 to +1.6 K, and − 0.8 to 0.0 K, respectively in the Southern Hemisphere. And 3) the a priori temperature and H_2O vertical profiles were taken from the official EUMETSAT IASI Level 2 products associated to the 2 × 15 pixels selected in favorable and unfavorable conditions (see Table 2 and Fig. 3); these profiles are shown in Figs. S5 and S6, respectively.

Figs. 4 and 5 illustrate the averaging kernels calculated for one pixel selected over France in favorable and unfavorable conditions, respectively. Note that the N_2O averaging kernels associated to the 2 × 15 pixels selected in favorable and unfavorable conditions (see Table 2 and Fig. 3) are shown in the Supplementary Material in Figs. S7 and S8, respectively. The averaging kernel represents the vertical sensitivity contained in the observations. Increasing the SNR from IASI and IASI-NG instruments to the ones of MIN_2OS increases the vertical sensitivity of the N_2O observations, with an obvious lower-tropospheric peak in MIN_2OS B1 and B2 during favorable conditions, even more pronounced in B2 than in B1 at 900 hPa. Three independent pieces of information are found at 300, 600 and, in favorable conditions, at 900 hPa. Whatever the conditions, retrievals in B3 show less sensitivity in the low troposphere compared to the ones in B1 and B2. The Degree-of-Freedom (DOF) characterizes the vertical information contained in the retrieval. In favorable conditions (Fig. 4), the DOFs in the MIN_2OS B1 and B2 reach ~2, while it is only 1.1–1.3 in IASI-NG; in B3, the MIN_2OS DOF is only 0.9–1.0 while the IASI-NG DOF is 0.5. In unfavorable conditions (Fig. 5), MIN_2OS DOFs in B1 and B2 (1.0–1.6) are still greater than IASI-NG DOFs (0.7–1.0) while, in B3, MIN_2OS DOFs are even much lower (0.2–0.5). From this analysis and the 2 × 15 pixels selected in favorable and unfavorable conditions (Figs. S7 and S8, respectively), we definitely rejected the band B3 to get valuable N_2O observations in the lower troposphere.

We kept the B1 and B2 bands in MIN_2OS for getting meaningful information on N_2O in the lowermost troposphere. We summarized the results obtained from MIN_2OS using the best configuration (SNR × 5) over the bands B1 and B2 in Fig. 6. We show the DOF (calculated from the surface to the top of the atmosphere), the DOF-600 (calculated from the surface to 600 hPa) to quantify the vertical information contained in the lowermost tropospheric retrieval, and the sensitivity of the averaging kernels (defined as the value of the averaging kernels at a given pressure) at 900 hPa in bands B1 and B2 for the 15 pixels in 2 conditions (favorable and unfavorable). Along the vertical, DOFs show a higher sensitivity in B1 (1.5–2.0) than in B2 (1.0–1.5) in unfavorable conditions and a similar sensitivity (2.0–2.5) in favorable conditions. However, in the lowermost troposphere, B2 provides more sensitivity (0.8–1.2) than B1 (0.6–1.0) while, in unfavorable conditions, sensitivity in B1 is slightly higher (0.4–0.6) than in B2 (0.2–0.5). This means that overall, in B1, the sensitivity in the upper troposphere is higher than in B2. This is also confirmed by our analyses focusing on 300 hPa. Fig. S9 shows a comparison of the MIN_2OS sensitivity of the averaging kernels considering a IASI-NG SNR × 5 between the bands at 1200 cm^{-1} (8 μm) and 2200 cm^{-1} (4 μm) for the 2 × 15 pixels (Fig. 3) in favorable (red and orange symbols) and unfavorable (dark and light blue symbols) conditions at

Table 1
Synthesis of the parameters setup in the TN_2OR V1.7 retrieval scheme as a function of the 3 bands B1, B2 and B3: a priori information and error for N_2O, CH_4, H_2O, O_3, CO_2, CO, temperature (T), surface temperature (T_s) and surface emissivity (ε).

N_2O		CH_4		H_2O		O_3		CO_2		CO		T		T_s		ε	
B1, B2, B3		B1		B1, B2, B3		B2		B2		B2		B1, B2, B3		B1, B2, B3		B1, B2, B3	
N_2O_{ap}	ΔN_2O	CH_{4ap}	ΔCH_4	H_2O_{ap}	ΔH_2O	O_{3ap}	ΔO_3	CO_{2ap}	ΔCO_2	CO_{ap}	ΔCO	T_{ap}	ΔT	T_{sap}	ΔT_s	ε_{ap}	Δε
HIPPO & LMDz	0.8%	MACC	2%	IASI	20%	MIPAS	30%	MIPAS	2%	MACC	20%	IASI	0.5 K	IASI	1.5 K	Atlas	0.15

Table 2
Location, latitude, longitude, date, time, day/night and surface pressure of the 2 × 15 MIN_2OS pixels used in our study measured in favorable (summer daytime) and unfavorable (winter nighttime) conditions.

Pixel #	Location	Latitude	Longitude	Date/2011	Time/UT	Day/Night	Surface P/hPa
1	Canada	58.03°N	118.08°W	17 July	17:58	Day	961.47
2		58.15°N	117.86°W	30 January	05:26	Night	991.3
3	North Atlantic Ocean	49.47°N	37.72°W	12 July	13:00	Day	1017.07
4		49.55°N	37.37°W	2 January	23:38	Night	1010.62
5	France	45.99°N	2.41°E	2 July	09:45	Day	934.47
6		46.12°N	2.45°E	19 January	21:03	Night	960.51
7	Spain	40.61°N	4.55°W	20 July	10:15	Day	893.73
8		40.58°N	4.4°W	2 January	21:54	Night	890.58
9	China	34.0°N	114.73°E	14 July	02:14	Day	1010.66
10		34.35°N	114.8°E	4 January	12:44	Night	1007.27
11	USA	33.12°N	92.82°W	18 July	16:03	Day	1000.56
12		32.81°N	92.83°W	6 January	03:34	Night	1019.15
13	Sahara	23.07°N	10.99°E	9 July	09:46	Day	915.74
14		23.07°N	10.88°E	6 January	20:25	Night	916.94
15	India	22.52°N	78.69°E	27 July	04:30	Day	950.05
16		22.46°N	78.36°E	8 January	16:20	Night	949.03
17	Maritime Continent	2.08°N	115.13°E	30 July	01:52	Day	904.86
18		0.54°N	116.49°E	5 January	13:54	Night	998.89
19	Amazonia	1.56°N	57.66°W	11 July	13:34	Day	982.17
20		1.74°N	57.43°W	12 January	01:20	Night	970.04
21	Equatorial Africa	4.99°S	21.94°E	4 January	08:22	Day	956.58
22		4.4°S	22.39°E	6 July	19:32	Night	948.33
23	Brazil	18.05°S	52.88°W	6 January	12:48	Day	923.44
24		19.13°S	57.05°W	4 July	01:35	Night	1014.21
25	Australia	26.08°S	133.12°E	7 January	00:39	Day	945.65
26		26.07°S	133.15°E	1 July	12:44	Night	956.67
27	South Africa	28.99°S	25.44°E	6 January	07:46	Day	878.57
28		29.11°S	25.64°E	1 July	19:29	Night	878.7
29	South Pacific Ocean	33.58°S	137.16°W	5 January	18:17	Day	1018.99
30		33.52°S	137.02°W	3 July	06:56	Night	1005.68

The 2 × 15 MIN_2OS pixels are also shown in Fig. 3.

900, 600 and 300 hPa. This clearly illustrates that overall, in B1, the sensitivity of the 300-hPa averaging kernels (0.25–0.30) is higher than in B2 (0.17–0.28). In the middle troposphere (600 hPa), the sensitivity of the averaging kernels in bands B1 and B2 is similar (0.20–0.25).The sensitivity of the 900-hPa averaging kernels is similar in B1 and B2 in unfavorable conditions (0.0–0.2) but, in favorable conditions, the sensitivity is higher in B2 (0.2–0.5) than in B1 (0.1–0.4). The theoretical analysis so far does not allow us to differentiate clearly, between the spectral bands B1 and B2, which one performs better in providing optimum information on N_2O in the lowermost troposphere for any condition. In Section 3, we present further results of the SNRs expected from actual detectors.

3. The MIN_2OS instrumental concept

3.1. Mission

The MIN_2OS instrument will be onboard a platform in synergy with 2 other platforms expected to fly in 2031–2032. It will fly in time and space coincidence with Metop-SG carrying IASI-NG and Sentinel-2 NG so as to use surface properties such as temperature and emissivity, vertical profiles of atmospheric constituents (pollutants, GHGs and aerosols) and temperature to optimally estimate N_2O vertical profiles in the retrieval procedure. Sentinel-2 NG will provide ancillary data on the soil, crop and management practices on the field scale, an added value to the N_2O surface fluxes inverted in the MIN_2OS project. Flying with Metop-SG constrains the altitude and the time of Equator crossing to about 830 km and 09:30 LT, respectively. The expected lifetime of the MIN_2OS project is 4–5 years in order to study the interannual variability of N_2O surface fluxes on the local and global scales for the first time.

3.2. Instrument configuration

To address major shortcomings in IASI and IASI-NG, namely a lack of information on N_2O in the lowermost troposphere, we propose a novel TIR satellite instrument. Instead of expecting that the Noise Equivalent delta Radiance (NEdL) could be decreased by a factor 3–5 compared to that of the IASI-NG as we showed in Section 2, we used the actual configurations (SNR and horizontal resolution) of a set of 4 detectors (see Fig. 9). At 1300 cm^{-1}, LYNRED/SCORPIO and TELEDYNE/GEOSNAP were chosen and, at 2200 cm^{-1}, we selected LYNRED/DAPHNIS and TELEDYNE/GEOSNAP. For both bands at any given horizontal resolution, the TELEDYNE detectors showed much less NEdL than the LYNRED detectors. Note that at 10-km resolution, the SNR associated with the 4 detectors was 4–7 times higher than the one from IASI-NG.

3.3. Instrument performance

We made calculations with TN_2OR, consistent with Section 2, only modifying the SNR to the one from the 4 detectors at a 10-km resolution, namely the lowest noise reachable, considering the same 15 pixels in favorable and unfavorable conditions. Fig. 7 shows the averaging kernel sensitivity vs the total error calculated at 300, 600 and 900 hPa for the 4 detectors in bands B1 and B2. On average, for any pressure level and band, the higher the sensitivity (ranging 0.0–0.7), the lower the total error (ranging 0.3–0.7%). At 300 and 600 hPa, the impact of the favorable conditions on the sensitivity and error is not obvious, except that the poorest sensitivity is always found in unfavorable conditions. At these two levels, on average, the sensitivity in B1 is slightly better than the sensitivity in band B2 by 0.2. Consistent with results obtained in Section 2.3, the sensitivity (and error) at 900 hPa: 1) is better by 0.4 in favorable than in unfavorable conditions and 2), in a given condition, is slightly better by 0.1–0.2 in band B2 than in band B1. As expected with the associated SNR, the sensitivity calculated with the TELEDYNE/GEOSNAP detectors is higher by 0.1–0.2 than the one calculated with the LYNRED/DAPHNIS and LYNRED/SCORPIO detectors.

However, several possible effects on the N_2O retrievals need to be addressed:

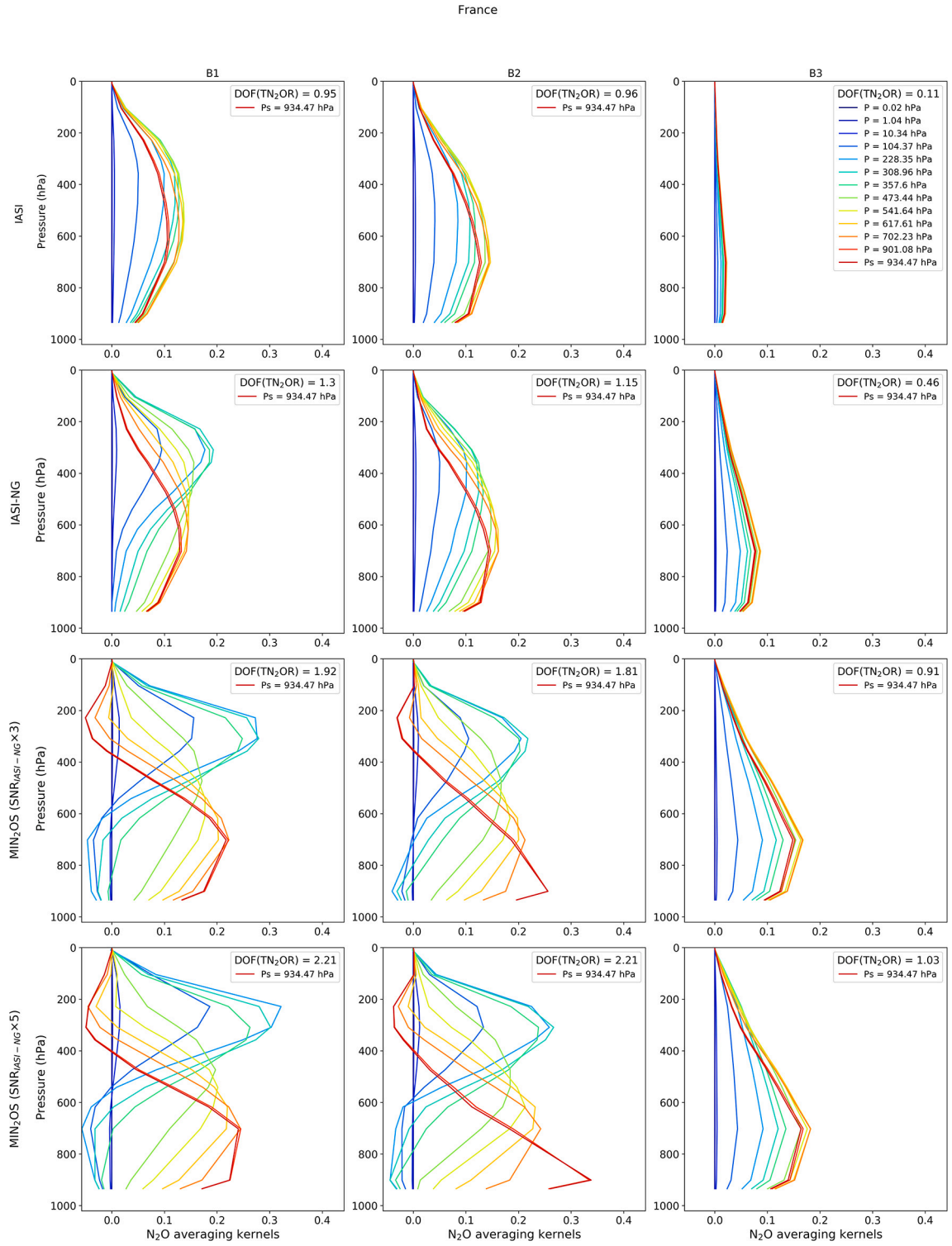

Fig. 4. N_2O averaging kernels calculated with TN_2OR for one pixel over France (see Fig. 3 and Table 2) in favorable conditions considering the 3 bands (B1, B2 and B3, from left to right) and 4 instrumental concepts (from top to bottom): IASI, IASI-NG, MIN_2OS (SNR IASI-NG × 3) and MIN_2OS (SNR IASI-NG × 5).

3.3.1. *Aerosol contamination*

The RTTOV model is able to consider aerosol impact on the IR radiances by using climatological vertical distributions of different types of aerosols. Aerosol information from the IASI spectra is now routinely retrieved (e.g., Clarisse et al., 2013; Cuesta et al., 2015) relying on the spectral band 750–1250 cm^{-1}. Sensitivity of aerosols in the LWIR and MWIR has been investigated with AIRS sensor (Peyridieu et al., 2010; updated in https://ara.lmd.polytechnique.fr/index.php?page=aerosols_old for IASI) considering mineral dust for aerosol optical depths (AODs) ranging 0.2–0.6: 1) above 1250 cm^{-1}, the impact of aerosol appears to be negligible (difference between clear sky radiance and aerosol-impacted radiance less than 0.2 K) while 2) between 2150 and 2260 cm^{-1}, aerosol has non-negligible effects on the radiance from 0.5 to 1.5 K, with its maximum impact around 2150 cm^{-1}.

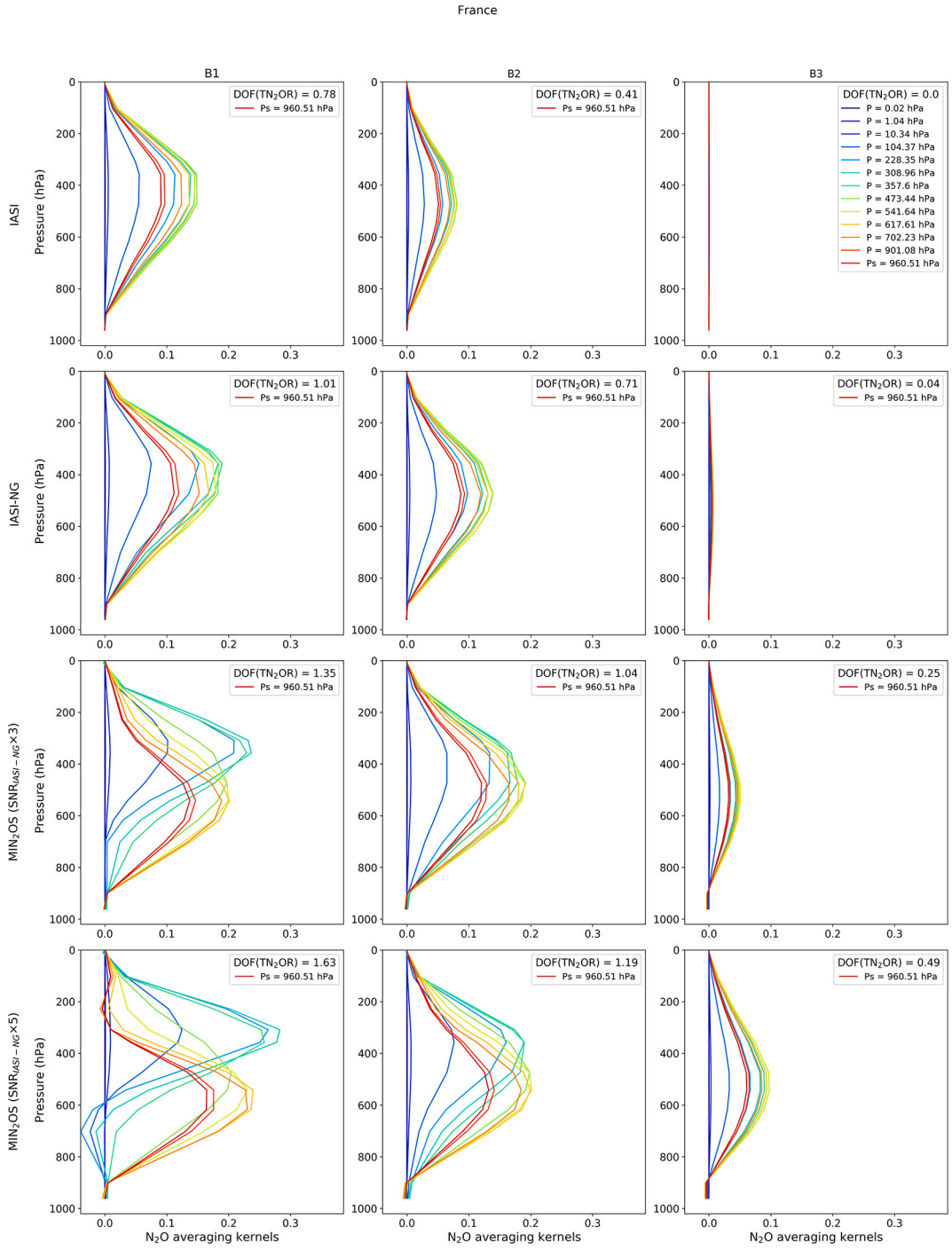

Fig. 5. Same as Fig. 4 but for one pixel over France (see Fig. 3 and Table 2) in unfavorable conditions.

3.3.2. *Non-Local Thermodynamic Effect (NLTE) effect*

The RTTOV model is also able to consider NLTE impact on the IR radiances. This effect is important in the 4 μm band. Since the N_2O lines are mixed with the CO_2 bands in this region, recent studies (Matricardi et al., 2018) have investigated this effect on daytime measurements. The difference between radiances with and without taking into account NLTE effects can reach 6 K around 2320 cm^{-1}, with a NLTE effect that is non-negligible over the region 2240–2390 cm^{-1}.

3.3.3. *Spectroscopy*

We are aware of some issues discussed in the community that will need to be investigated theoretically and in the laboratory by the group during phases 0 and A: 1) line mixing in the region around the Q-branch at 1306 cm^{-1}, 2) accuracy of the spectroscopic parameters describing the Voigt shape and their temperature dependence, and 3) contribution/overlap of CH_4 lines with those of N_2O.

3.3.4. *Retrieval*

1) Contamination of the retrieved species other than N_2O onto N_2O retrieval errors: the retrieval contamination issues have already been tackled when retrieving N_2O from IASI radiances with TN_2OR V1.7. For MIN_2OS, we have evaluated the contamination factor (Chalinel et al., 2021) on the N_2O estimation induced by the parameters to be simultaneously retrieved. In band B1, H_2O and CH_4 impacted the N_2O total

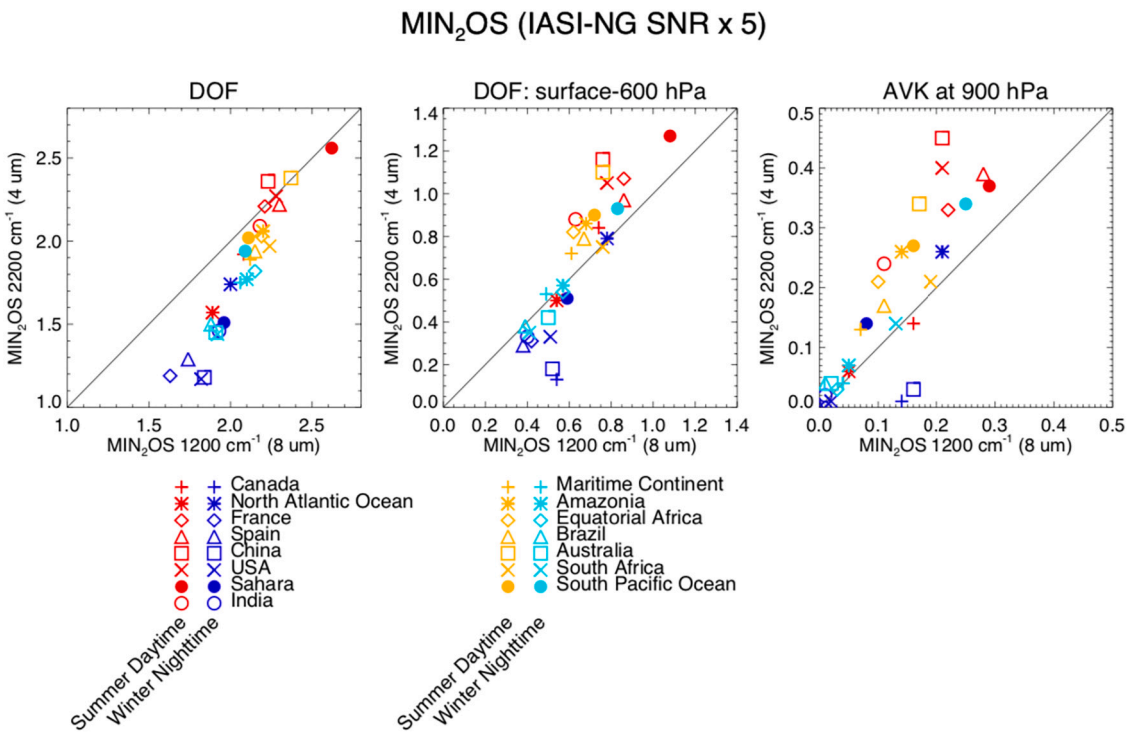

Fig. 6. Comparison of the MIN_2OS sensitivity considering a IASI-NG SNR × 5 between the bands at 1200 cm^{-1} (8 μm) and 2200 cm^{-1} (4 μm) for the 2 × 15 pixels (Fig. 3) in favorable (red and orange symbols) and unfavorable (dark and light blue symbols) conditions: (left) DOF (calculated from the surface to the top of the atmosphere), (middle) lowermost tropospheric DOF (calculated from the surface to 600 hPa) and (right) sensitivity of the averaging kernels at 900 hPa. (For interpretation of the references to colour in this figure legend, the reader is referred to the web version of this article.)

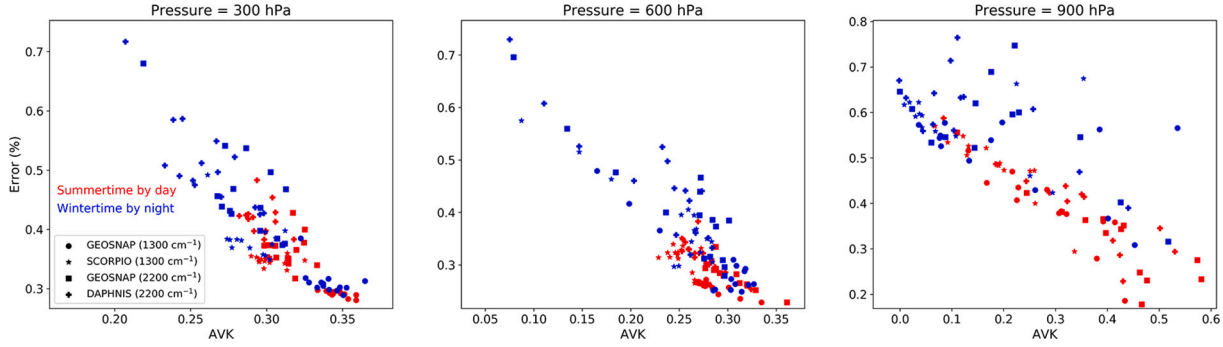

Fig. 7. Averaging kernel sensitivity vs total error calculated over the 2 × 15 pixels in favorable (summer daytime, red) and unfavorable (winter nighttime, blue) conditions at 300 (left), 600 (centre) and 900 hPa (right) considering the NEdL associated with the 4 detectors with a 10-km horizontal resolution: LYNRED/SCORPIO (star) and TELEDYNE/GEOSNAP (circle) at 1300 cm^{-1}, LYNRED/DAPHNIS (plus) and TELEDYNE/GEOSNAP (square) at 2200 cm^{-1}. (For interpretation of the references to colour in this figure legend, the reader is referred to the web version of this article.)

error by 0.1–0.3% (Fig. 8). Similarly, in band B2, H_2O, O_3 and CO impacted the N_2O total error by ~0.7% (not shown). 2) Systematic errors (detectors, temperature, spectroscopy) will need to be specifically investigated when adapting our TN_2OR tool to the MIN_2OS final specifications during phases 0 and A. As a consequence, to minimize aerosol contamination and NLTE effect on the radiances, we reduced the total bandwidth of the 2 bands to B1 (1250–1330 cm^{-1}) and B2 (2150–2240 cm^{-1}).

3.4. Instrument and project specification synthesis

In summary, using highly-sensitive detectors, three independent pieces of information in the N_2O vertical profile could be obtained within the MIN_2OS project by retrieving the radiances measured in both bands B1 (1250–1330 cm^{-1}) and B2 (2150–2240 cm^{-1}): at 900 hPa (specific to MIN_2OS), 600 hPa (middle troposphere same as with IASI-NG and GOSAT-2) and 300 hPa (upper troposphere same as with IASI, IASI-NG, GOSAT and GOSAT-2). The standard deviation error on one single pixel of 10 × 10 km^2 is calculated to be lower than the one estimated for IASI and GOSAT, namely less than 1% at all levels, reaching 0.2–0.8% (0.8–2.7 ppbv) at 900 hPa. The N_2O observation in the lowermost troposphere is highly dependent on the conditions encountered: over land, with high sensitivity in favorable conditions, such as in summer daytime, and low sensitivity in unfavorable conditions, such as in winter nighttime, and, over the ocean, opposite to over land. For information, since one configuration has been chosen to develop the MIN_2OS technical concept focusing on B1 with a GEOSNAP detector, we show the associated averaging kernel, total error and contamination factor (as defined in Chalinel et al., 2021) averaged over the 15 pixels considered in favorable and unfavorable conditions (Fig. 8). Averaging

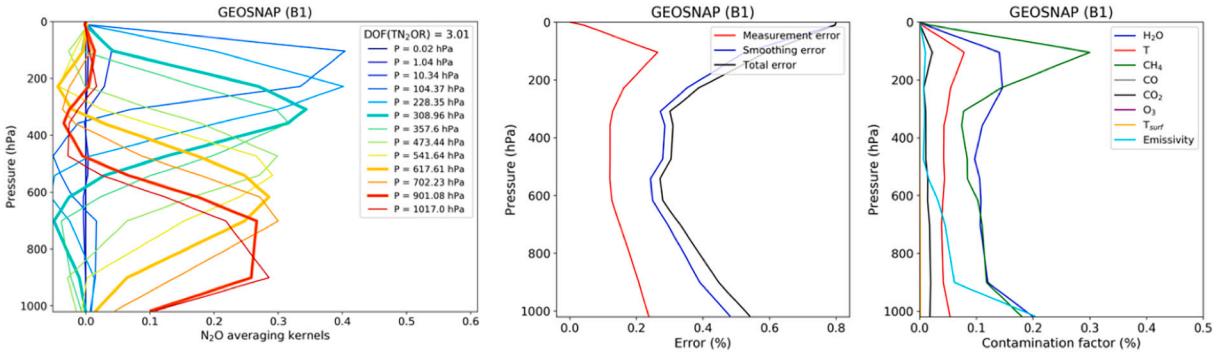

Fig. 8. (Left) Averaging kernel sensitivity, (center) total error (%) and (right) contamination factor (%) calculated over the 2 × 15 pixels in favorable and unfavorable conditions with the GEOSNAP detector in band B1.

kernels peak at 900 hPa, with a DOF ~3, a total error < 1% and mainly 2 constituents (H_2O and CH_4 and, to a lesser extent, surface emissivity) contaminate N_2O in the lowermost troposphere (0.1–0.2%).

4. The MIN$_2$OS system solution

4.1. The MIN$_2$OS optical payload

Our theoretical study (Section 3) shows that two bands can be used to optimally retrieve N_2O in the lowermost troposphere at 8 (B1) and 4 μm (B2). In the present study, we have considered both bands and several detectors. The main instrument is an imaging spectrometer composed of an entrance telescope, a slit, and a spectrometer made of a collimator, a diffraction grating, imaging optics and a detection module. The instrument is sized to provide a horizontal resolution of 10 km from an altitude close to 800 km. In complement to the spectrometer, a wide field and high horizontal resolution TIR imager is implemented for cloud detection with an improved spatial resolution of 1 km. The two instruments are sharing a common calibration system including calibration blackbody. Several design options have been investigated for the spectrometer, with two candidate spectral bands suitable to the mission objectives, at 4 and 8 μm. Several candidate detectors have been analyzed, providing different instrument characteristics and radiometric performance levels.

4.1.1. Main instrument requirements

Two candidate spectral bands are considered at mission level: spectral band B1, centered on 1290 cm^{-1}, and spectral band B2, centered on 2205 cm^{-1}. The spectral resolution requirement is based on the IASI-NG spectral resolution of 0.25 cm^{-1}, with an oversampling factor of 2. The resulting resolving power is 5160 for B1 and 8820 for B2. The selected orbit is based on the Sentinel-2 orbit (786 km); the required horizontal resolution is below 10 km, with a minimum swath width at least equal to Sentinel-2 MSI (290 km). The radiometric noise requirement is set at a reference temperature of 280 K, with a Noise Equivalent differential Temperature (NEdT) about five times lower than the IASI-NG requirement, for a spatial sampling distance of 10 km. The MIN$_2$OS payload will also include a cloud imager to discard cloudy and/or partly-cloudy pixels. The actual analysis was performed by considering cloud-free pixels only.This imager must operate in the TIR band in order to be operational during day and night. The instrument technology is using a microbolometer array operated near ambient conditions.

4.1.2. Candidate detector arrays

4.1.2.1. Spectral band B1. Three detector arrays have been identified as possible candidate to cover the spectral band B1: the SCORPIO and DAPHNIS arrays from Lynred, and the GEOSNAP array from Teledyne. The SCORPIO LongWave InfraRed (LWIR) is a 640 × 512 pixels IR detector produced by Lynred since 2010. The DAPHNIS LWIR corresponds to DAPHNIS MidWave InfraRed (MWIR) ROIC coupled to Lynred LWIR photodiodes. Despite its large format (1280 × 720 pixels), a full frame rate as high as 85 Hz can be reached thanks to the implementation of digital output, offering 80 Mpixel/s output rate. The GEOSNAP/CHROMA-D corresponds to a family of 18-μm pixel pitch MCT IR detectors developed by Teledyne US mainly for Earth Observation from space.

4.1.2.2. Spectral band B2. Two detector arrays have been identified as possible candidate to cover the spectral band B2: the DAPHNIS array from Lynred, and the GEOSNAP array from Teledyne. The DAPHNIS MWIR ROIC for band B2 is similar to the DAPHNIS LWIR ROIC described above. GEOSNAP for B2 is similar to the one proposed for B1 except that MWIR MCT p/n photodiodes are used, offering an even larger Technology Readiness Level (TRL) (≥ 6) thanks to ongoing space programs (e.g., the James Webb Space Telescope) using similar 18-μm pitch MWIR photodiode technology.

4.1.2.3. Cloud Imager. The uncooled detector technology is selected for the Cloud Imager. The PICO1024Gen2 is a COTS microbolometers 2D array manufactured by Lynred, featuring a 1024 × 768-pixels format with a 17-μm pixel pitch.

4.1.3. Cooling system

Considering the requested spectrometer and detector temperature, active cooling is a robust solution e.g. with fully qualified Air Liquid LPTC two-stage pulse-tube cooler, already implemented on IASI-NG. Alternatively, active detector cooling with its IDDCA, combined with spectrometer passive cooling may be considered, especially in case of nadir pointing only.

4.2. Optical performance

4.2.1. Optical quality

All instrument design cases provide very good optical quality with spot diagrams RMS diameter smaller than the pixel size, with values well below the Airy diameter.

4.2.2. Cloud Imager

The cloud imager consists in a refractive camera combined with a microbolometer detector array operating at ambient temperature. The PICO 1024 array from Lynred is selected: the array features 1024 × 768 pixels at 17-μm pitch.

4.3. Radiometric performances

4.3.1. Spectrometer

The radiometric performances have been estimated using a signal-to-

noise model of the instrument including typical optical transmission data and detector characteristics. The instrument is operating in push-broom mode.

4.3.2. Instrument operating temperature

The required detector and spectrometer temperatures have been determined to provide a limited contribution to the overall noise budget according to the available detector noise models. The operating temperature of the Teledyne array is about 10 K higher than for the Lynred arrays.

4.3.3. Noise budget

The detector array and spectrometer temperatures have been determined to provide noise contributors consistent with the photonic signal levels. Typical models have been used. The gain factor of 5 with regard to IASI-NG is so achievable in most of the cases, with significant margin using the GEOSNAP array (Fig. 9).

4.3.4. Cloud imager

The radiometric performances are estimated using the Airbus internal performance model of the PICO 1024 detector array. We consider an along-track spatial sampling equal to the native spatial resolution, i.e., 0.333 km.

4.4. Implementation

A tentative accommodation of the instrument on a platform has been performed to get an estimate of the required satellite resources (Fig. 10). For this exercise, the spectral band B1 has been considered, on the basis of the GEOSNAP array, which corresponds to the largest instrument case. The spectrometer optics are mounted on a main baseplate. The optics are split into two units: the telescope and collimator unit, and the imaging optics unit. The TIR camera and the spectrometer share the same calibration mechanism.

4.5. Instrument properties

Table 3 synthesizes the instrument budget: mass, volume, power, etc.

5. The MIN_2OS mission

5.1. The MIN_2OS orbit

The mission is directly driven by the need to fly in convoy mode with Metop-SG embedding IASI-NG. Considering that both ocean and land have to be covered and that imaging is performed both during day and night, Fig. 11 illustrates the resulting mission performances of the system. As a result, all land is accessed both in day and night conditions over the complete 29 days of orbital cycle.

Regarding satellite operations, the MIN_2OS mission is simple and repetitive, which allows us to implement a simple operation scheme, with limited frequency of Telemetry, Tracking & Command contacts (typically once every few days). Regarding the payload data download, the amount of data to be downloaded is particularly limited. But the payload data latency required may be short, in the order of 5–10 h. This implies that payload data would potentially have to be downloaded almost every orbit, which would be a significant constraint on the payload ground station antennas network selection.

5.2. MIN_2OS platform and satellite configuration

The MIN_2OS satellite is dedicated to a single imaging spectrometer instrument. The satellite design is driven by the instrument design, the need to acquire images continuously over the orbit (including night time), the minimization of development risks through an extensive reuse of already developed and validated elements and the end of life deorbitation.

5.2.1. MIN_2OS platform built around Astrobus avionics

The platform identified to best suit the MIN_2OS mission will be built around the Astrobus standard avionics. AstroBus is Airbus' Low Earth Orbit (LEO) avionics product. It comprises a suite of flight hardware, software, documentation, test benches and tools, implemented and managed as an avionics product. It is maintained to adopt improvements/issues from individual projects, shared and addressed for the benefit of current and future projects. Projects based on an avionics product benefit from proven elements already developed, validated and flown together.

5.2.2. Satellite configuration

The payload is directly accommodated on the top floor of the platform, as shown in Fig. 12. The platform is a simple box-shaped structure, with a stable top floor to be used for platform interface. The star trackers can be mounted on the top floor for improved pointing performances. With respect to the accommodation, a great care is brought to ensuring the feasibility of harness installation, satellite accessibility, testability and dismountability. Scientific data downlink is ensured in X-band, thanks to the moderate data volume generated by the instrument. The proposed platform product can easily be customized with a Ka-band system such as the one baselined for Copernicus LSTM. All other functional chains (electrical power, S-band, payload data handling and transmission, propulsion) are defined in the AstroBus standard, and fulfill all the needs and performance requirements of the MIN_2OS mission. The modular central software is also part of the platform product, and is designed so as to be easily adapted to any mission.

Such a platform largely covers the 5 years lifetime as required as a minimum by the mission. The suitability of a standard platform designed for Earth Observation is confirmed thanks to MIN_2OS main mission

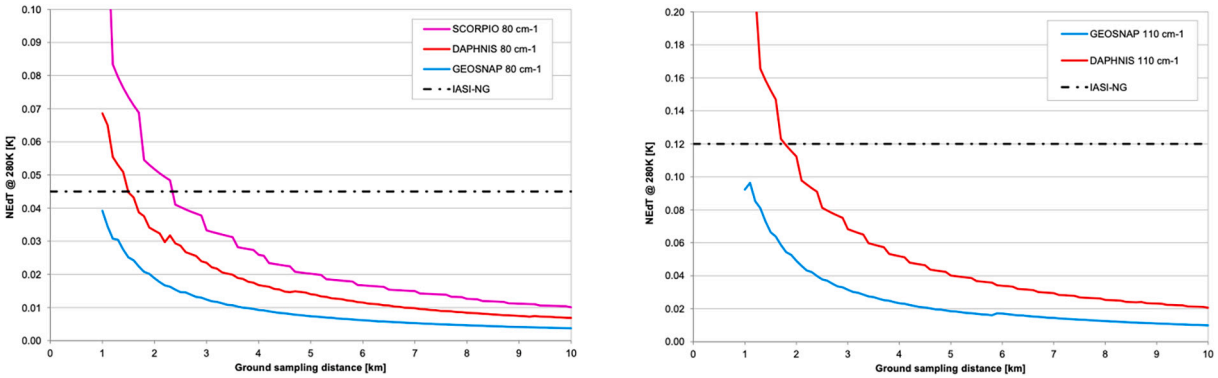

Fig. 9. Noise Equivalent differential Temperature (NEdT) @ 280 K as a function of the ground spatial sampling distance in band B1 (left) and B2 (right).

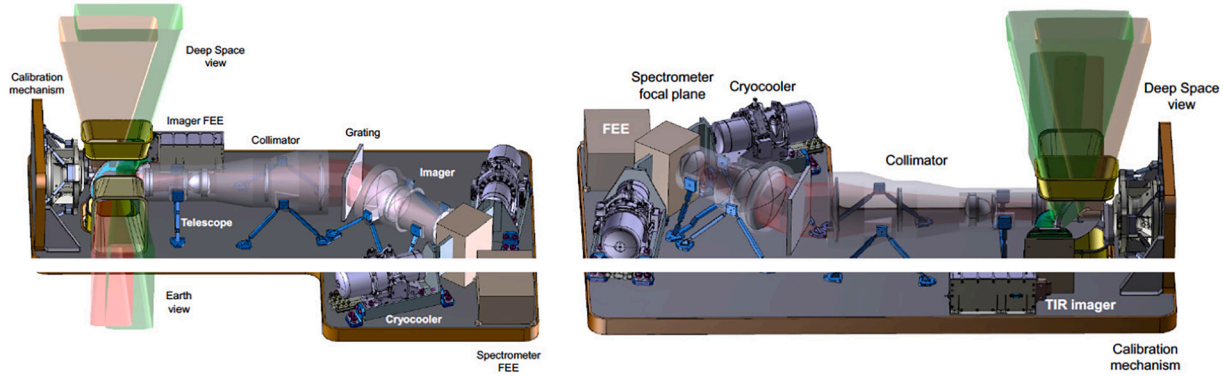

Fig. 10. Instrument accommodation.

Table 3
Synthesis of the instrument properties: mass, volume, power and data rate.

Property	Value
Mass	91.4 kg
Volume	1200 × 600 × 300 mm^3
Power	167 W
Data Rate	200 MBits/s (spectro) & 6.4 kbits/s (camera)

requirements. The constant power demand from the instrument is lower than that of other high-resolution instruments. The permanent nadir pointing offers a stable thermal environment, and does not put agility constraints on the attitude control subsystem. Finally, fair pointing stability and geolocation requirements are a consequence of the instrument 10-km resolution, and can be easily ensured with the proposed platform class.

VEGA-C launcher is considered as the reference launcher. More specifically the presented configuration is largely compatible with VESPA-C from volume point of view, thus offering the possibility to have a co-passenger to largely limit launch costs. Also, the Sun Synchronous 09:30 LT at Descending Node is a common orbit giving many possibilities of compatibility with other satellites as co-passenger.

A total mass budget of 430 kg has been estimated. The propellant budget was computed with the following assumptions: 1) altitude of 820 km with a reference surface of 10 m^2, 2) ISP of 210 s (hydrazine), and 3) 7 years lifetime, assumption of worst-case phasing with solar activity.

6. N_2O sources

6.1. Source inversion

N_2O fluxes can be estimated by TD approaches from observations of N_2O mixing ratio assimilated into an atmospheric inversion system (e.g., Huang et al., 2008; Thompson et al., 2014; Bergamaschi et al., 2015; Thompson et al., 2019). Up to now, however, inversions had to rely on sparse ground-based networks owing to the lack of satellite observations with the necessary sensitivity and precision. Our innovative TD approach will use space-borne observations of N_2O vertical profiles over land and ocean, with sensitivity to the lowermost troposphere around 800 hPa, going down to 900 hPa in favorable conditions such as in summer during daytime (see Section 3). We will develop the capacity for global- and regional-scale inverse modelling using satellite N_2O retrievals. We will use existing Chemical Transport Models (CTMs) and their adjoint models. One of the candidate models for the global scale is Laboratoire de Météorologie Dynamique (LMDz5), which is used for the Copernicus Atmosphere Monitoring Service (CAMS) N_2O inversions and currently has a horizontal resolution of 3.75° × 1.875° (Thompson et al., 2019). We will increase the horizontal resolution to 1° × 1° and incorporate the assimilation of satellite data of N_2O. For the regional scale, candidate models are the Eulerian CTM, CHIMERE (Menut et al., 2013), and the Lagrangian particle dispersion model, FLEXible PARTicle dispersion model (FLEXPART; Pisso et al., 2019) for high resolution (10 × 10 km^2) inversions (Fig. 13 left). The models will be driven with meteorological reanalyses from European Centre for Medium-Range Weather Forecasts (ECMWF), such as the new ECMWF Reanalyses v5

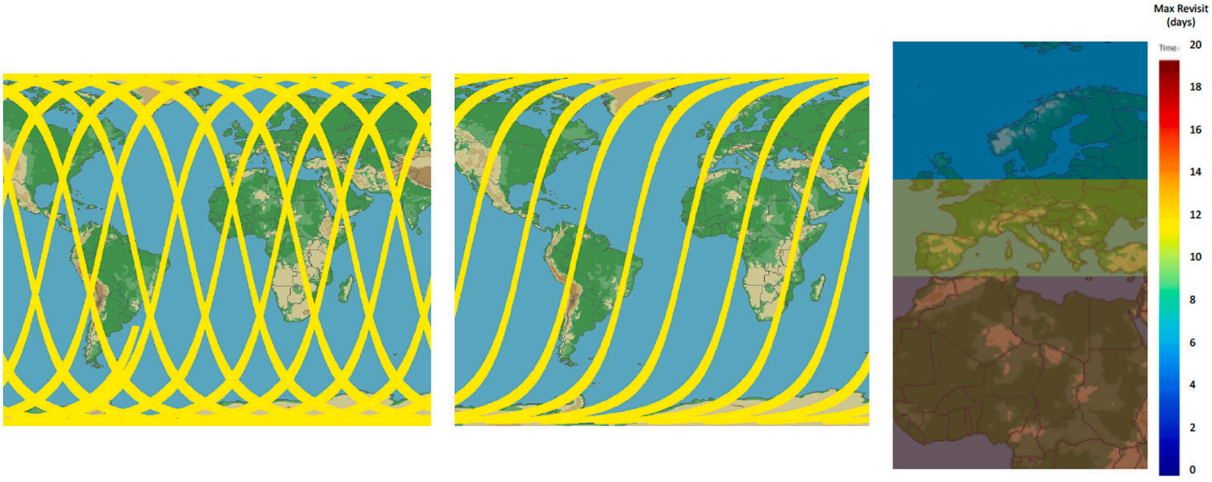

Fig. 11. Mission performance illustration: (left) areas observed over 1 day and considering both ascending and descending orbits visibilities, (center) considering only descending orbits visibilities and (right) maximum revisit delays considering only descending orbits (ascending case would give the same results).

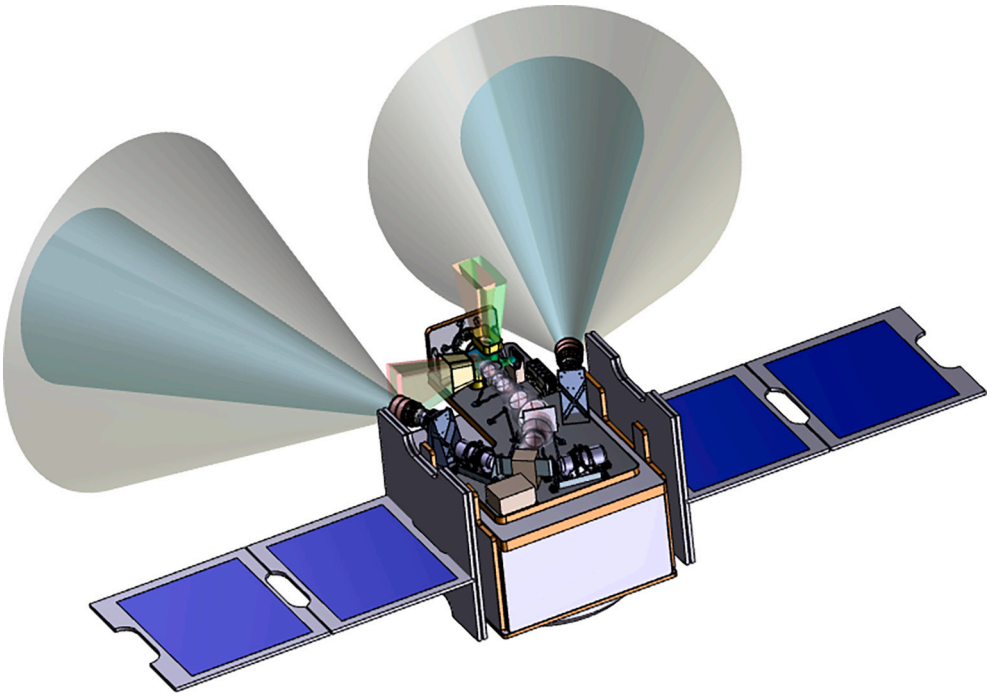

Fig. 12. Imaging spectrometer instrument accommodation on AstroBus platform.

(ERA5) reanalysis available hourly at a 30-km horizontal resolution for global-scale modelling, and the High RESolution (HRES) analysis data available hourly at a 10-km resolution for regional-scale modelling.

For all CTMs, the optimization will be based on Bayesian statistics and will use existing optimization algorithms, such as the Quasi-Newton algorithm, M1QN3. Furthermore, we will make use of the new Community Inversion Framework (CIF), which is an open-source Python toolbox for atmospheric inversions, developed in the framework of the H2020 project VERIFY (Berchet et al., 2020), and we will further contribute to its development, especially in terms of the assimilation of high-resolution satellite data. The CIF is based on the PyVAR system used for N_2O (Thompson et al., 2014; Bergamaschi et al., 2015; Thompson et al., 2019), CO_2 (Chevallier et al., 2010; Broquet et al., 2011; Chevallier et al., 2014; Monteil et al., 2020), CH_4 (Pison et al., 2009; Cressot et al., 2014; Bergamaschi et al., 2015; Pison et al., 2018) and CO and NOx (Fortems-Cheiney et al., 2019). The CIF is already interfaced with the CTMs: LMDz5 (global scale), FLEXPART (global and regional scales) and CHIMERE (regional scale). It includes the variational inversion method (among other methods) and can be used to assimilate satellite data, as well as surface measurements. It is currently used for projects dealing with GHGs (H2020 VERIFY (https://verify.lsce.ipsl.fr/) and CHE (https://che-project.eu/) projects and the French Agence Nationale de la Recherche (ANR) ARGONAUT project (https://anr.fr/Project-ANR-19-CE01-0007)) as well as reactive species (H2020 VERIFY, and the French ANR projects ARGONAUT and POLEASIA (http://www.lisa.u-pec.fr/projets/?id=1269)). An advantage of using different CTMs is the possibility to assess the impact of atmospheric transport errors in the posterior fluxes.

We show two examples of N_2O source inversions. Firstly, a technical demonstration of the source inversion system CIF set up to assimilate

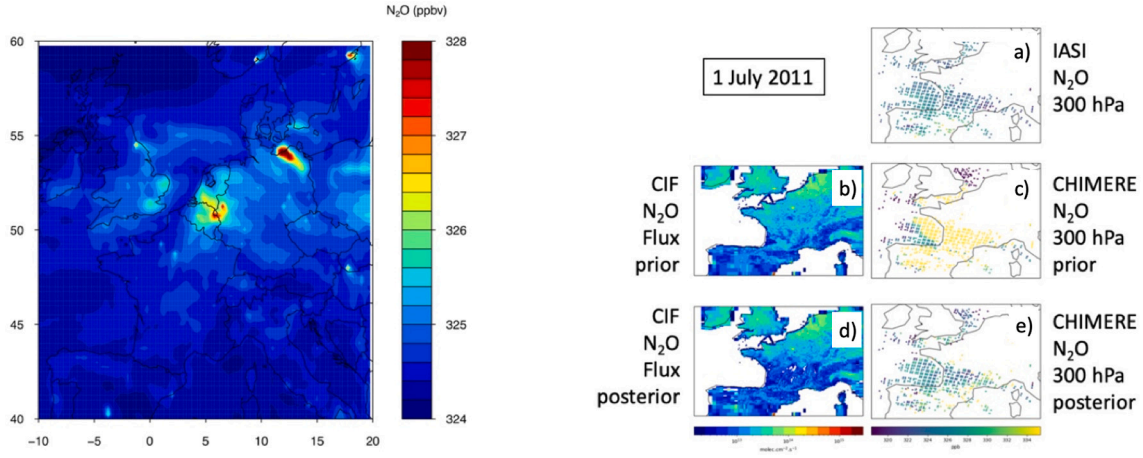

Fig. 13. (Left) Surface N_2O as calculated by FLEXPART in July 2011 over Europe at 25-km resolution. Some of the N_2O hotspots are industrial sources, namely nitric acid plants (e.g. in northeast Germany, Sweden and Norway) and not agricultural sources. (Right) Source inversion system CIF set-up to assimilate IASI TN_2OR observations at 300 hPa on 1 July 2011 (a) into CHIMERE in a domain covering France at a 10 × 10 km^2 horizontal resolution. From the prior N_2O fluxes (b) by EDGAR v5, the prior equivalents of the observations are simulated by CHIMERE (c). After 10 iterations, the posterior fluxes (d) and concentrations at 300 hPa (e) are obtained.

IASI TN_2OR observations at 300 hPa on 1 July 2011 into CHIMERE in a domain covering France at a 10×10 km^2 horizontal resolution is shown Fig. 13 right. From the prior N_2O fluxes (b) by Emissions Database for Global Atmospheric Research (EDGAR) v5 (Crippa et al., 2019), the prior equivalents of the observations are simulated (c). The source inversion system minimizes the differences between the observations (a) and the simulations (c) by correcting the prior fluxes (b). After 10 iterations, the posterior fluxes (d) and the concentrations at 300 hPa (e) simulated with the posterior fluxes are obtained. The reduction of the differences between the posterior concentrations (e) and the observations (a) shows that the inversion system behaves optimally. Secondly, the PyVAR-CAMS system has assimilated over the period of July 2011: 1) in a first inversion, the NOAA N_2O surface observations, 2) in a second inversion, the IASI TN_2OR N_2O Total Columns over land and daytime, and 3) in a third inversion, the IASI TN_2OR N_2O Total Columns over land and the ocean during daytime and nighttime. The uncertainty reduction in the surface fluxes shows the actual impact of the observations onto the inverted fluxes. The uncertainty reduction is calculated as one minus the ratio of the posterior to prior uncertainty for each grid cell. The posterior uncertainty is calculated using a Monte Carlo ensemble of inversions each with a perturbed prior according to the method of Chevallier (2007). When using NOAA surface data, the uncertainty reduction can reach high values (~50%) over areas where surface observations are available (Northern America, Europe and East Asia) (Fig. 14 top left) but is very weak (<5%) over the tropics, subtropics and southern hemisphere owing to a lack of observations. When using IASI space-borne observations over land and daytime, the uncertainty reduction is on average greater than 10% over land and could reach high values (~25%) over the tropics (South America, Africa, India, South-East Asia) in areas where surface observations are not available (Fig. 14 bottom left).

When using all IASI observations (land/ocean and daytime/nighttime), the uncertainty reduction is on average similar to the uncertainty reduction obtained when assimilating only IASI ocean/daytime observations (Fig. 14 top right) although slightly smaller (~20%) except at high latitudes (Siberia and Canada) and over the ocean where it is greater (25–30%). Note again the lack of observations over these particular regions, which underlines the complementarity of spaceborne and surface observations.

The impact of assimilating either NOAA or IASI observations over land/daytime or over land/ocean/daytime/nighttime on the surface flux in a synthetic data experiment is shown in Fig. 15. Consistent with uncertainty reduction maps, the N_2O fluxes are mainly modified in the Northern Hemisphere over land, where the NOAA sites are located, when assimilating surface observations while, when using the IASI observations, the N_2O fluxes are also impacted in the tropics and over the Indian sub-continent. There is consistency between IASI- and NOAA-derived N_2O flux adjustments over USA and Siberia and Eastern China only when considering IASI daytime data. The negative adjustment in N_2O flux observed in NOAA data over Eastern Canada is not present in the IASI data, and the positive adjustment in NOAA-derived N_2O flux observed in NOAA data over Europe is not so high in the IASI data. The real impact of space-borne observations on the derived surface flux compared to surface observations is over South America, Equatorial Africa, the Indian sub-continent and South-East Asia and Australia. The "true" pattern of flux differences (labelled as "Reference") shows basically the same distribution as the ones calculated with IASI and NOAA data but with amplitudes significantly larger by a factor 2–3 on average.

6.2. Modelling

The seasonal variability of modelled surface N_2O demonstrates how limited our knowledge is about the processes affecting tropospheric N_2O, which represents the combined effects of surface fluxes as well as atmospheric transport and chemistry. The same N_2O inventories were used in three state-of-the-art CTMs (LMDz5, FLEXPART and Model for Interdisciplinary Research on Climate – version 4 (MIROC-4, Patra et al., 2018)) to examine the impact of modelled transport on tropospheric N_2O variability for the year 2011 (Fig. 16). Especially at high latitudes, the models have difficulties in capturing the phase and amplitude of the observed seasonality (Fig. 16 left). The annual mean meridional gradient in surface N_2O with respect to the South Pole station (Fig. 16 right) is underestimated by the models (~1.25 ppbv in the models and ~ 1.75 ppbv in NOAA data from the South Pole to 30°N) suggesting an underestimate of the tropical and northern hemisphere sources in the inventory.

In Fig. 17, global-scale distributions of N_2O horizontal variability taken from IASI TN_2OR V1.7 (Chalinel et al., 2021) in July 2011 also reveal higher values (+3%) at 300 hPa over the tropics (with local maximum over Africa) than at high latitudes (−3%). This variability is reduced in the PyVAR-CAMS inversion products with tropical maxima of +1% (no local maximum over Africa) and minima of −1% at high latitudes.

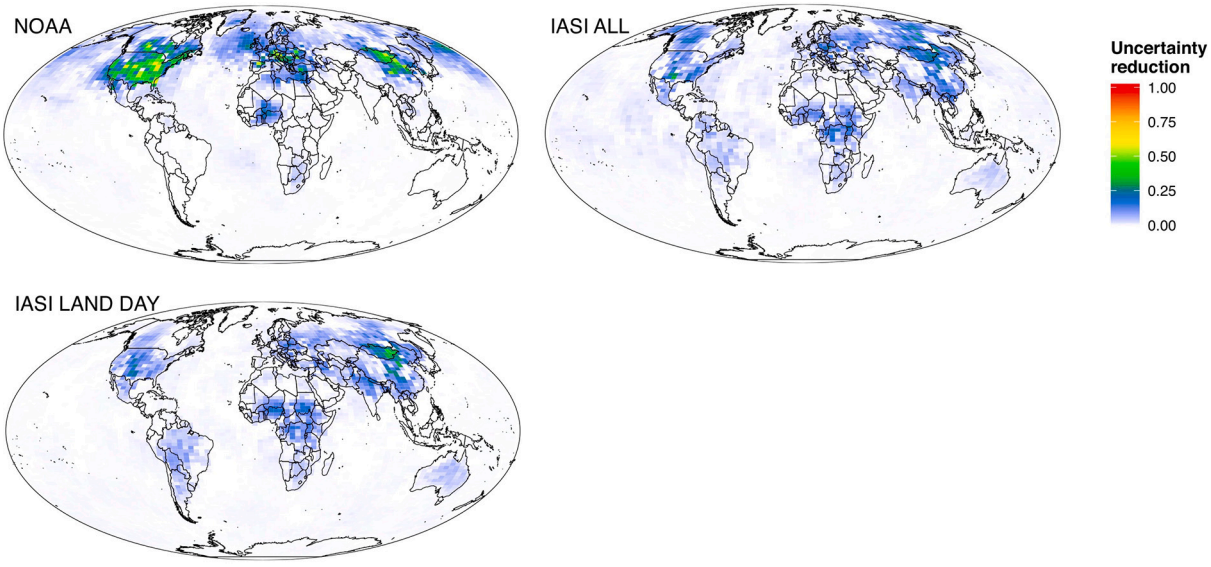

Fig. 14. Uncertainty reduction (0–1) in the N_2O surface flux obtained in PyVAR-CAMS when assimilating (top left) NOAA N_2O surface observations, (bottom left) IASI TN_2OR N_2O Total Columns over land during daytime, (top right) IASI TN_2OR N_2O Total Columns over land and the ocean during daytime and nighttime in July 2011.

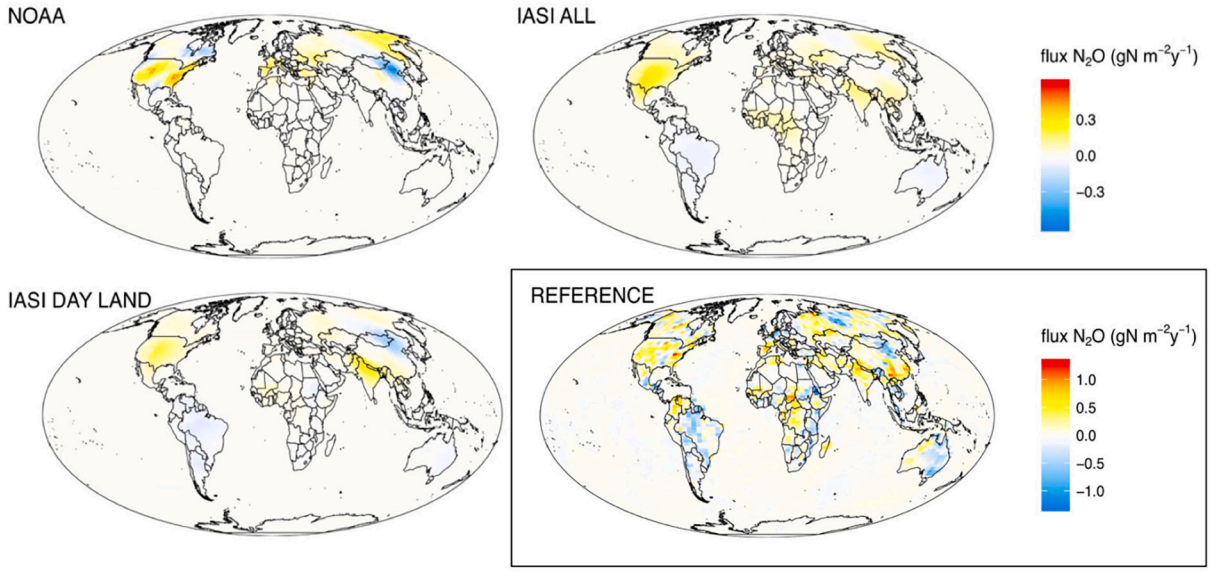

Fig. 15. Impact on the N_2O surface flux obtained by PyVAR-CAMS in a synthetic data experiment when assimilating (top left) NOAA N_2O surface observations, (bottom left) IASI TN_2OR N_2O Total Columns over land and daytime, (top right) IASI TN_2OR N_2O Total Columns over land, ocean, daytime and nighttime in July 2011. The "true" pattern of flux differences (labelled as "Reference") is presented in the bottom right panel with a colour table different from the 3 other panels.

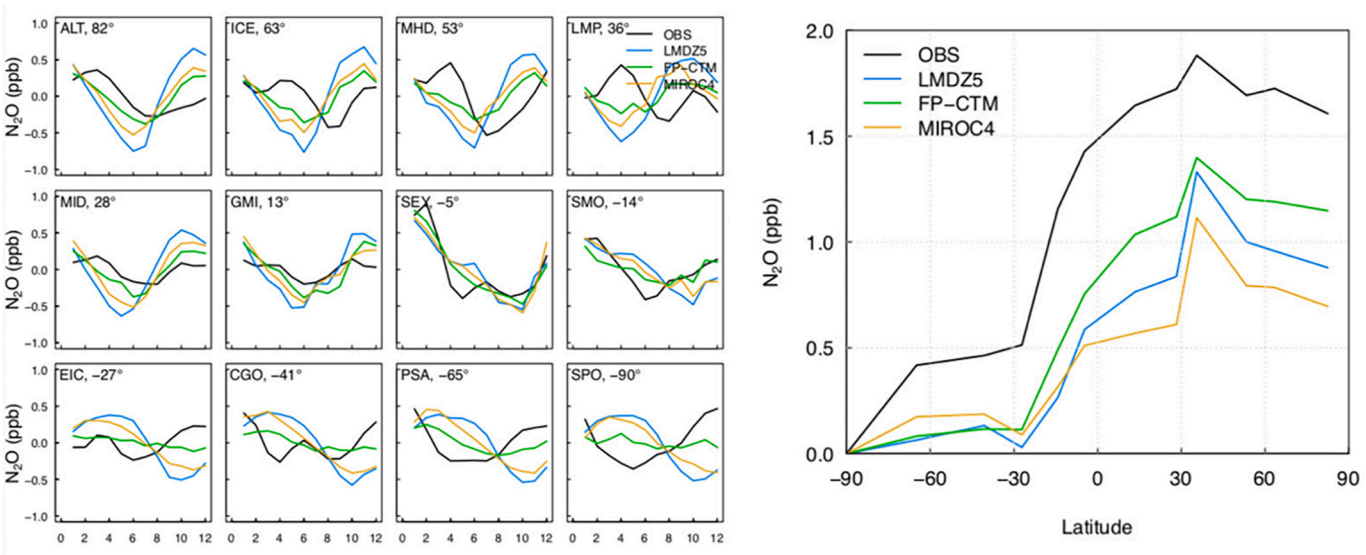

Fig. 16. (Left) Seasonal cycle of N_2O measured at the surface of 12 stations in 2011 (black) and calculated by LMDz (blue), FLEXPART (green) and MIROC-4 (orange) from the northern to the southern high latitudes. (Right) Observed and calculated annual mean meridional gradient in surface N_2O with respect to the South Pole station. (For interpretation of the references to colour in this figure legend, the reader is referred to the web version of this article.)

A process-based model will be used to calculate local to regional N_2O fluxes from agroecosystems on a daily basis. The STICS soil-crop model (Brisson et al., 1998; Bergez et al., 2014) describes and integrates biophysical-chemical processes related to the functioning of the agricultural cropping systems which accounts for agricultural management practices. The majority of process-based models that can predict N_2O emissions (e.g., STICS; DeNitrification-DeComposition (DNDC), Giltrap et al., 2010; Daily Century (DayCent), Del Grosso et al., 2005) have daily outputs. Being one dimensional, they need to run on actual or conceptual homogeneous sub-units in term of soil, crop and management practices. Insofar that spatial databases of soil properties, crop identification and associated management practices are available, they can provide explicit regional N_2O emission predictions in response to climatic conditions. STICS crop model has a built-in capability of reinitializing missing spatial information such as seeding dates, seeding density and soil moisture at field capacity using leaf area index derived from satellite observations such as Landsat or Sentinel-2 (e.g., Jégo et al., 2012, 2015). Therefore, it can be run for large agricultural regions using relevant soil, crop, and climate databases.

6.3. *Validation*

The validation of space-borne atmospheric N_2O is a difficult process since there is a lack of N_2O observations in the troposphere, the vast majority of atmospheric N_2O measurements being at the surface (ground-based sites) and in the stratosphere (satellites). Nevertheless, aircraft campaigns (e.g., HIAPER Pole-to-Pole Observations (HIPPO); National Oceanic and Atmospheric Administration (NOAA) and Atmospheric Tomography Mission (ATOM), National Aeronautics and Space Administration (NASA)), ground-based networks using Fourier-

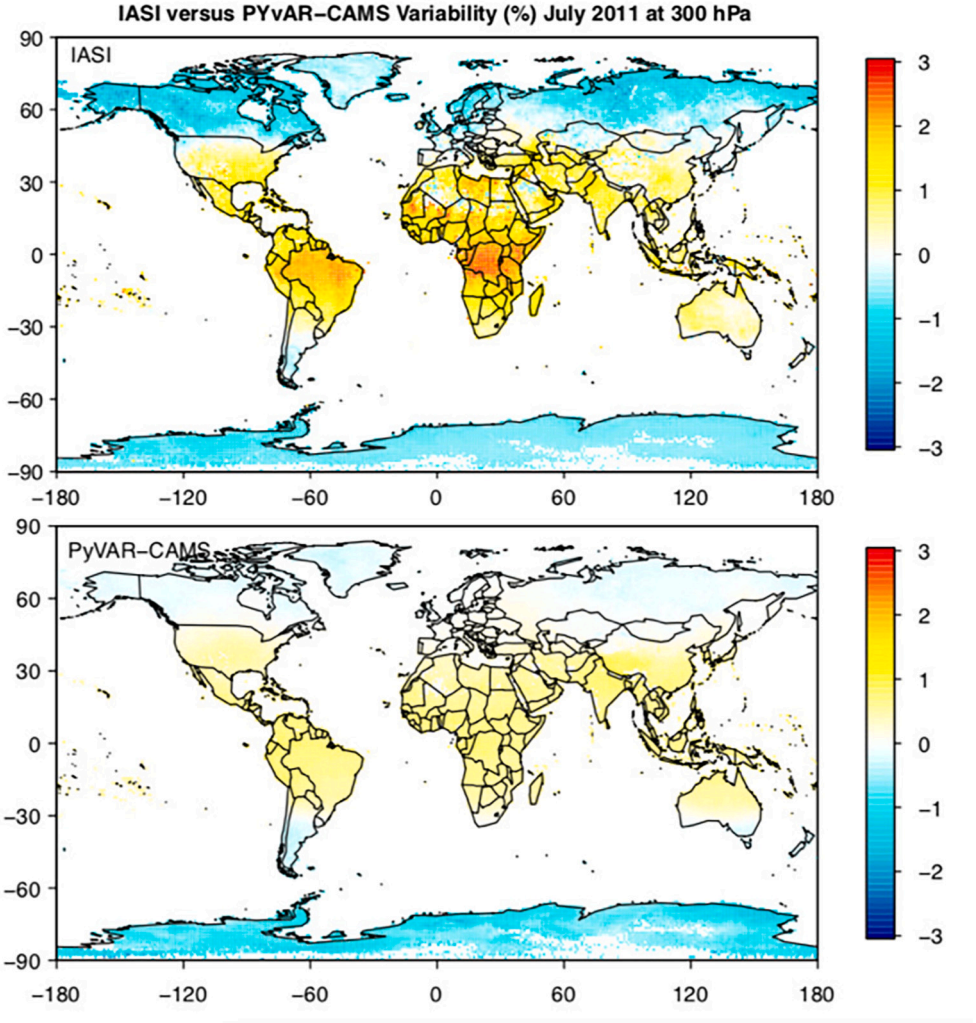

Fig. 17. Horizontal distribution of the monthly-averaged variability of N_2O at 300 hPa from IASI TN_2OR V1.7 (Chalinel et al., 2021) within 1° × 1° pixels (top) and in PyVAR-CAMS model (bottom) in July 2011.

transform infrared spectroscopy (FTIR) detectors (e.g., Network for the Detection of Atmospheric Composition Change, NDACC; Total Carbon Column Observing Network, TCCON), and space-borne observations (e.g., GOSAT-2, IASI-NG) will help assessing the quality of MIN_2OS observations. As an example, retrievals of IASI TN_2OR N_2O at 300 hPa have been compared with HIPPO and NOAA airborne observations (Chalinel et al., 2021). On average, IASI N_2O behaved consistently with HIPPO and NOAA data (correlations of 0.65–0.68), a bias of 1.52–1.87 ppbv but a higher variability (by a factor 2) is found in IASI data compared to HIPPO and NOAA data.

Surface N_2O fluxes and vertical N_2O profiles obtained within the MIN_2OS project will be validated against in situ surface measurements obtained within the Integrated Carbon Observation System (ICOS)-Atmosphere and ICOS-Ecosystem networks, the Network for the Detection of Atmospheric Composition Change (NDACC), the AirCore innovative atmospheric sampling system, together with coincident space-borne observations (e.g., IASI-NG on MetOp-SG). Dedicated campaigns in Germany and Italy could be organized through the Modelling European Agriculture with Climate Change for Food Security (MACSUR) initiative.

7. Conclusions

The MIN_2OS project aims at monitoring nitrous oxide (N_2O) sources on the global scale at a spatial resolution of 1° × 1° and on the regional scale at a high spatial resolution (10 × 10 km^2) by inverting surface fluxes from N_2O space-borne measurements sensitive to the lowermost atmospheric layers under favorable conditions. The emission inventories of N_2O provided by MIN_2OS will contribute to quantifying the Earth's radiative forcing on the global scale and on a weekly to monthly basis depending on the application (e.g., agriculture, national inventories, policy, scientific research). Our novel approach is based on the development of: 1) a space-borne instrument operating in the TIR domain inherited from a more sensitive version of the Infrared Atmospheric Sounding Interferometer (IASI) and the Infrared Atmospheric Sounding Interferometer-New Generation (IASI-NG) instruments, providing N_2O mixing ratio, in clear sky conditions, in the lowermost atmosphere (900 hPa) under favorable conditions (summer daytime) over land and under favorable and unfavorable (winter nighttime) conditions over the ocean and 2) an inversion source model to estimate, from atmospheric satellite observations, N_2O surface fluxes.

To fulfill the MIN_2OS objectives, a new TIR instrument will be developed. Our study shows that two bands can be used to optimally retrieve N_2O in the lowermost troposphere at 8 (spectral band B1) and 4 μm (spectral band B2) with 4 highly-sensitive detectors (signal-to-noise at least better by a factor 5 than the one of IASI-NG). Our scientific requirements can be reached whatever the detector and the band used. The MIN_2OS baseline instrument will finally be centered on the N_2O spectral band B1 at 1250–1330 cm^{-1}, with a resolution of 0.125 cm^{-1}, a Full Width at Half Maximum of 0.25 cm^{-1} and a swath of 300 km. It will be on-board a platform at ~830 km altitude crossing the Equator in

descending node at 09:30 local time in synergy with 2 other platforms expected to fly in 2031–32: 1) in time and space coincident with Metop-SG that will contain IASI-NG to use surface properties and vertical profiles of atmospheric constituents and temperature to optimally constrain the retrieval of N_2O vertical profiles and 2) with Sentinel-2 NG to use agricultural surface information on the field scale (crop types, area, management practices) with no need of synchronization. The lifetime of the MIN$_2$OS project could be 4–5 years to study the inter-annual variability of N_2O surface fluxes. In this configuration, the spectral noise can be decreased by at least a factor 5 compared to the lowest noise accessible to date with the IASI-NG and the Greenhouse gases Observing SATellite-2 (GOSAT-2) missions. The horizontal resolution is expected to be $1^\circ \times 1^\circ$ on the global scale and 10×10 km^2 on the regional scale, consistent with the resolution of state-of-the-art regional transport and source inversion models. With the MIN$_2$OS project, N_2O will be obtainable from three separate atmospheric layers: in the lowermost troposphere around 900 hPa (specific to MIN$_2$OS), in the middle troposphere around 600 hPa (like IASI-NG and GOSAT-2) and in the upper troposphere around 300 hPa (like IASI, IASI-NG and GOSAT-2). The N_2O total random error is expected to be less than ~1% (~3 ppbv) along the vertical, reaching 0.2–0.6% at 900 hPa in favorable conditions.

The main instrument is an imaging spectrometer operating at 8 μm and composed of an entrance telescope, a slit and a spectrometer made of a collimator, a diffraction grating, an imager and a detection module. It provides a swath of 300 km and a resolution of 10×10 km^2. The instrument dimensioning is largely driven by the requirement to have a signal-to-noise that is at least better than a factor 5 compared to the one of IASI-NG. The preliminary design of the MIN$_2$OS project results in a small instrument (payload of 90 kg, volume of $1200 \times 600 \times 300$ mm^3) with, in addition to the spectrometer, a wide field and 1-km resolution imager desirable for cloud detection. It results in a possible accommodation of the instrument(s) on a small platform, the whole satellite being largely compatible with a dual launch on VEGA-C. The main trade-offs on spectrometer design are at the level of detector technology (preliminary baseline is a TELEDYNE GEOSNAP 2048 × 1024 matrix), reflective or refractive optical design (preference for refractive design), optical material, slit, active or passive cooling, selection of grating technology.

The source inversion system will be based on the Community Inversion Framework, using CTMs that include photochemical loss of N_2O in the stratosphere. Globally, we aim at a global horizontal resolution of $1^\circ \times 1^\circ$ for the source inversion, which will be a significant improvement of the current state-of-the-art of $\sim 3^\circ \times 2^\circ$. In addition, we will use regional CTMsfor source inversions with a high target resolution of 10×10 km^2. Maps of N_2O flux analyses will be provided at a weekly to monthly time resolution for several years, and will be used to estimate national and regional scale emissions. With accurate emission estimates from the TD approach together with land-biosphere models to estimate the natural sources, we aim at reducing the uncertainties of the anthropogenic emissions on the national scale. Local N_2O fluxes from agricultural fields will also be predicted using the 1-D process-based crop model (STICS), developed for a large range of crops and cropping systems and adapted in various agricultural regions of the world (Europe, Canada, Asia, Africa). Vertical profiles of N_2O will be validated against measurements from international networks as well as dedicated intensive field campaigns.

The MIN$_2$OS project will produce the expertise needed for producing high spatiotemporal resolution N_2O fluxes, which will be delivered to the user community (research scientists, agricultural policy makers, and other stakeholders) and will help verify the implementation and impact of policies and support international initiatives such as the IPCC and the Paris Agreement. We expect that the N_2O flux estimates from MIN$_2$OS will facilitate management strategies, e.g., by optimizing agricultural management practices to minimize N_2O emissions, and mitigate emissions of this important GHG. The MIN$_2$OS project was submitted to the European Space Agency (ESA) Earth Explorer 11 (EE11) mission ideas.

Funding and acknowledgements

The TN$_2$OR project is funded by the Région Occitanie, the University of Toulouse, the Institut National des Sciences de l'Univers (INSU)/ Centre National de la Recherche Scientifique (CNRS), Météo-France, the Centre National d'Etudes Spatiales (CNES), Airbus Defense and Space, and Sciences et technologies pour l'Aéronautique et l'Espace (STAE) foundation. RC's PhD has been funded by Région Occitanie and Airbus Defense and Space. We would like to thank the three anonymous reviewers for their beneficial comments.

Declaration of Competing Interest

The authors declare no conflict of interest.

Appendix A. Supplementary data

Supplementary data to this article can be found online at https://doi.org/10.1016/j.rse.2021.112688.

References

Alves, B.J., Smith, K.A., Flores, R.A., Cardoso, A.S., Oliveira, W.R., Jantalia, C.P., Urquiaga, S., Boddey, R.M., 2012. Selection of the most suitable sampling time for static chambers for the estimation of daily mean N_2O flux from soils. Soil Biol. Biochem. 46, 129–135. https://doi.org/10.1016/j.soilbio.2011.11.022.

Bakker, D.C., Bange, H.W., Gruber, N., Johannessen, T., Upstill-Goddard, R.C., Borges, A. V., Delille, B., Löscher, C.R., Naqvi, S.W.A., Omar, A.M., Santana-Casiano, J.M., 2014. Air-sea interactions of natural long-lived greenhouse gases (CO_2, N_2O, CH_4) in a changing climate. In: Liss, P.S., Johnson, M.T. (Eds.), Ocean-Atmosphere Interactions of Gases and Particles, pp. 113–169.

Berchet, A., Sollum, E., Thompson, R.L., Pison, I., Thanwerdas, J., Broquet, G., Chevallier, F., Aalto, T., Bergamaschi, P., Brunner, D., Engelen, R., Fortems-Cheiney, A., Gerbig, C., Groot Zwaaftink, C., Haussaire, J.-M., Henne, S., Houweling, S., Karstens, U., Kutsch, W.L., Luijkx, I.T., Monteil, G., Palmer, P.I., van Peet, J.C.A., Peters, W., Peylin, P., Potier, E., Rödenbeck, C., Saunois, M., Scholze, M., Tsuruta, A., Zhao, Y., 2020. The Community Inversion Framework v1.0: a unified system for atmospheric inversion studies. Geosci. Model Dev. Discuss. https://doi.org/10.5194/gmd-2020-407 in review.

Bergamaschi, P., Corazza, M., Karstens, U., Athanassiadou, M., Thompson, R.L., Pison, I., Manning, A.J., Bousquet, P., Segers, A., Vermeulen, A.T., Janssens-Maenhout, G., Schmidt, M., Ramonet, M., Meinhardt, F., Aalto, T., Haszpra, L., Moncrieff, J., Popa, M.E., Lowry, D., Steinbacher, M., Jordan, A., O'Doherty, S., Piacentino, S., Dlugokencky, E., 2015. Top-down estimates of European CH_4 and N_2O emissions based on four different inverse models. Atmos. Chem. Phys. 15, 715–736. https://doi.org/10.5194/acp-15-715-2015.

Bergez, J.E., Raynal, H., Launay, M., Beaudoin, N., Casellas, E., Caubel, J., Chabrier, P., Coucheney, E., Dury, J., Garcia de Cortazar-Atauri, I., Justes, E., Mary, B., Ripoche, D., Ruget, F., 2014. Evolution of the STICS crop model to tackle new environmental issues: new formalisms and integration in the modelling and simulation platform RECORD. Environ. Model. Softw. 62, 370–384.

Brisson, N., Mary, B., Ripoche, D., Jeuffroy, M.H., Ruget, F., Nicoullaud, B., Gate, P., Devienne-Barret, F., Antonioletti, R., Dürr, C., Richard, G., Beaudoin, N., Recous, S., Tayot, X., Plenet, D., Cellier, P., Machet, J.M., Meynard, J.-M., Delécolle, R., 1998. STICS: a generic model for the simulation of crops and their water and nitrogen balances. I. Theory and parameterization applied to wheat and corn. Agronomie 18 (5–6), 311–346.

Broquet, G., Chevallier, F., Rayner, P., Aulagnier, C., Pison, I., Ramonet, M., Schmidt, M., Vermeulen, A.T., Ciais, P., 2011. A European summertime CO_2 biogenic flux inversion at mesoscale from continuous in situ mixing ratio measurements. J. Geophys. Res. Atmos. 116, D23303 https://doi.org/10.1029/2011JD016202.

Chalinel, R., Attié, J.-L., Ricaud, P., Vidot, J., Kangah, Y., Hauglustaine, D., Thompson, R. L., 2021. Global-scale observation and evaluation of nitrous oxide from IASI on MetOp-A. Submitted to Remote Sens. Environ. Special Issue: Remote Sensing of Greenhouse Gas Emissions, under review.

Charteris, A.F., Chadwick, D.R., Thorman, R.E., Vallejo, A., de Klein, C.A., Rochette, P., Cárdenas, L.M., 2020. Global research alliance N_2O chamber methodology guidelines: recommendations for deployment and accounting for sources of variability. J. Environ. Qual. 49 (5), 1092–1109. https://doi.org/10.1002/jeq2.20126.

Chevallier, F., 2007. Impact of correlated observation errors on inverted CO_2 surface fluxes from OCO measurements. Geophys. Res. Lett. 34, 24. https://doi.org/10.1029/2007GL030463.

Chevallier, F., Feng, L., Bösch, H., Palmer, P.I., Rayner, P.J., 2010. On the impact of transport model errors for the estimation of CO_2 surface fluxes from GOSAT observations. Geophys. Res. Lett. 37, L21803 https://doi.org/10.1029/2010GL044652.

Chevallier, F., Palmer, P.I., Feng, L., Boesch, H., O'Dell, C.W., Bousquet, P., 2014. Toward robust and consistent regional CO_2 flux estimates from in situ and spaceborne measurements of atmospheric CO_2. Geophys. Res. Lett. 41, 1065–1070. https://doi.org/10.1002/2013GL058772.

Clarisse, L., Coheur, P.F., Prata, F., Hadji-Lazaro, J., Hurtmans, D., Clerbaux, C., 2013. A unified approach to infrared aerosol remote sensing and type specification. Atmos. Chem. Phys. 13 (4), 2195–2221.

Clerbaux, C., Boynard, A., Clarisse, L., George, M., Hadji-Lazaro, J., Herbin, H., Hurtmans, D., Pommier, M., Razavi, A., Turquety, S., Wespes, C., Coheur, P.-F., 2009. Monitoring of atmospheric composition using the thermal infrared IASI/MetOp sounder. Atmos. Chem. Phys. 9, 6041–6054. https://doi.org/10.5194/acp-9-6041-2009.

Cressot, C., Chevallier, F., Bousquet, P., Crevoisier, C., Dlugokencky, E.J., Fortems-Cheiney, A., Frankenberg, C., Parker, R., Pison, I., Scheepmaker, R.A., Montzka, S.A., Krummel, P.B., Steele, L.P., Langenfelds, R.L., 2014. On the consistency between global and regional methane emissions inferred from SCIAMACHY, TANSO-FTS, IASI and surface measurements. Atmos. Chem. Phys. 14, 577–592. https://doi.org/10.5194/acp-14-577-2014.

Crevoisier, C., Clerbaux, C., Guidard, V., Phulpin, T., Armante, R., Barret, B., Camy-Peyret, C., Chaboureau, J.-P., Coheur, P.-F., Crépeau, L., Dufour, G., Labonnote, L., Lavanant, L., Hadji-Lazaro, J., Herbin, H., Jacquinet-Husson, N., Payan, S., Péquignot, E., Pierangelo, C., Sellitto, P., Stubenrauch, C., 2014. Towards IASI-New Generation (IASI-NG): impact of improved spectral resolution and radiometric noise on the retrieval of thermodynamic, chemistry and climate variables. Atmos. Meas. Tech. 7, 4367–4385. https://doi.org/10.5194/amt-7-4367-2014.

Crippa, M., Guizzardi, D., Muntean, M., Schaaf, E., Lo Vullo, E., Solazzo, E., Monforti-Ferrario, F., Olivier, J., Vignati, E., 2019. EDGAR v5.0 Greenhouse Gas Emissions. European Commission, Joint Research Centre (JRC) [Dataset] PID. http://data.europa.eu/89h/488dc3de-f072-4810-ab83-47185158ce2a.

Cuesta, J., Eremenko, M., Flamant, C., Dufour, G., Laurent, B., Bergametti, G., Höpfner, M., Orphal, J., Zhou, D., 2015. Three-dimensional distribution of a major desert dust outbreak over East Asia in March 2008 derived from IASI satellite observations. J. Geophys. Res. Atmos. 120 (14), 7099–7127.

Davidson, E.A., Kanter, D., 2014. Inventories and scenarios of nitrous oxide emissions. Environ. Res. Lett. 9, 105012.

De Klein, C., Novoa, R.S.A., Ogle, S., Smith, K.A., Rochette, P., Wirth, T.C., McConkey, B. G., Mosier, A., Rypdal, K., Walsh, M., Williams, S.A., 2006. N_2O emissions from managed soils, and CO_2 emissions from lime and urea application. In: IPCC Guidelines for National Greenhouse Gas Inventories, Prepared by the National Greenhouse Gas Inventories Programme, pp. 1–54.

Del Grosso, S.J., Mosier, A.R., Parton, W.J., Ojima, D.S., 2005. DAYCENT model analysis of past and contemporary soil N_2O and net greenhouse gas flux for major crops in the USA. Soil Tillage Res. 83, 9–24.

Desjardins, R.L., Pattey, E., Smith, W.N., Worth, D., Grant, B., Srinivasan, R., MacPherson, J.I., Mauder, M., 2010. Multiscale estimates of N_2O emissions from agricultural lands. Agric. Forest Meteorol. 150, 817–824.

Ehrhardt, F., Soussana, J.F., Bellocchi, G., Grace, P., McAuliffe, R., Recous, S., Sándor, R., Smith, P., Snow, V., de Antoni Migliorati, M., Basso, B., Bhatia, A., Brilli, L., Doltra, J., Dorich, C.D., Doro, L., Fitton, N., Giacomini, S.J., Grant, B., Harrison, M. T., Jones, S.K., Kirschbaum, M.U.F., Klumpp, K., Laville, P., Léonard, J., Liebig, M., Lieffering, M., Martin, R., Massad, R.S., Meier, E., Merbold, L., Moore, A.D., Myrgiotis, V., Newton, P., Pattey, E., Rolinski, S., Sharp, J., Smith, W.N., Wu, L., Zhang, Q., 2017. Assessing uncertainties in crop and pasture ensemble model simulations of productivity and N_2O emissions. Glob. Change Bio. 1–14. https://doi.org/10.1111/gcb.13965.

Fortems-Cheiney, A., Pison, I., Dufour, G., Broquet, G., Berchet, A., Potier, E., Coman, A., Siour, G., Costantino, L., 2019. Variational regional inverse modeling of reactive species emissions with PYVAR-CHIMERE. Geosci. Model Dev. Discuss. https://doi.org/10.5194/gmd-2019-186.

Giltrap, D.L., Li, C., Saggar, S., 2010. DNDC: a process-based model of greenhouse gas fluxes from agricultural soils. Agric. Ecosyst. Environ. 136, 292–300.

Grant, R.F., Pattey, E., 1999. Mathematical modelling of nitrous oxide emissions from an agricultural field during spring thaw. Glob. Biogeochem. Cycles 13 (2), 679–694.

Grant, R.F., Pattey, E., 2003. Modelling variability in N_2O emissions from fertilized agricultural fields. Soil Biol. Biochem. 35 (2), 225–243.

Hocking, J., Rayer, P., Rundle, D., Saunders, R., Matricardi, M., Geer, A., Brunel, P., Vidot, J., 2015. RTTOV v11 Users Guide. NWP SAF.

Huang, J., Golombek, A., Prinn, R., Weiss, R., Fraser, P., Simmonds, P., Dlugokencky, E. J., Hall, B., Elkins, J., Steele, P., Langenfelds, R., Krummel, P., Dutton, G., Porter, L., 2008. Estimation of regional emissions of nitrous oxide from 1997 to 2005 using multinetwork measurements, a chemical transport model, and an inverse method. J. Geophys. Res. Atmos. 113, D17313 https://doi.org/10.1029/2007JD009381.

IPCC, 2007. Guidelines for National Greenhouse Gas Inventories. http://www.ipcc-nggip.iges.or.jp/public/2006gl/.

IPCC, 2019. Refinement to the 2006 IPCC Guidelines for National Greenhouse Gas Inventories. https://www.ipcc.ch/report/2019-refinement-to-the-2006-ipcc-guidelines-for-national-greenhouse-gas-inventories.

Jégo, G., Pattey, E., Liu, J., 2012. Using Leaf Area Index, retrieved from optical imagery, in the STICS crop model for predicting yield and biomass of field crops. Field Crop Res. 131, 63–74.

Jégo, G., Pattey, E., Mesbah, S.M., Liu, J., Duchesne, I., 2015. Impact of the spatial resolution of climatic data and soil physical properties on regional corn yield predictions using the STICS crop model. Int. J. Appl. Earth Obs. Geoinf. 41, 11–22.

Kangah, Y., Ricaud, P., Attié, J.L., Saitoh, N., Hauglustaine, D.A., Wang, R., El Amraoui, L., Zbinden, R., Delon, C., 2017. Summertime upper tropospheric nitrous oxide over the Mediterranean as a footprint of Asian emissions. J. Geophys. Res. Atmos. 122 https://doi.org/10.1002/2016JD026119.

Kurata, O., Iki, N., Matsunuma, T., Inoue, T., Tsujimura, T., Furutani, H., Kobayashi, H., Hayakawa, A., 2017. Performances and emission characteristics of NH_3–air and NH_3/CH_4–air combustion gas-turbine power generations. Proceed. Combus. Inst. 36, 3351–3359. https://doi.org/10.1016/j.proci.2016.07.088.

Levenberg, K., 1944. A method for the solution of certain nonlinear problems in least squares. Q. Appl. Math. 2, 164.

Loveless, M., Borbas, E.E., Knuteson, R., Cawse-Nicholson, K., Hulley, G., Hook, S., 2021. Climatology of the combined ASTER MODIS emissivity over land (CAMEL) version 2. Remote Sens. 13, 111. https://doi.org/10.3390/rs13010111.

Marquardt, D.W., 1963. An algorithm for least-squares estimation of nonlinear parameters. SIAM J. Appl. Math. 11, 431.

Matricardi, M., 2009. Technical Note: an assessment of the accuracy of the RTTOV fast radiative transfer model using IASI data. Atmos. Chem. Phys. 9, 6899–6913. https://doi.org/10.5194/acp-9-6899-2009.

Matricardi, M., López-Puertas, M., Funke, B., 2018. Modeling of nonlocal thermodynamic equilibrium effects in the classical and principal component-based version of the RTTOV fast radiative transfer model. J. Geophys. Res. Atmos. 123 (11), 5741–5761.

Menut, L., Bessagnet, B., Khvorostyanov, D., Beekmann, M., Blond, N., Colette, A., Coll, I., Curci, G., Foret, G., Hodzic, A., Mailler, S., Meleux, F., Monge, J.-L., Pison, I., Siour, G., Turquety, S., Valari, M., Vautard, R., Vivanco, M.G., 2013. CHIMERE 2013: a model for regional atmospheric composition modelling. Geosci. Model Dev. 6, 981–1028. https://doi.org/10.5194/gmd-6-981-2013.

Metivier, K.A., Pattey, E., Grant, R.F., 2009. Using the Ecosys mathematical model to simulate temporal variability of nitrous oxide emissions from a fertilized agricultural soil. Soil Biol. Biochem. 41, 2370–2386.

Minschwaner, K., Salawitch, R.J., McElroy, M.B., 1993. Absorption of solar radiation by O_2: implications for O_3 and lifetimes of N_2O, $CFCl_3$, and CF_2Cl_2. J. Geophys. Res. Atmos. 98 (D6), 10543–10561.

Monteil, G., Broquet, G., Scholze, M., Lang, M., Karstens, U., Gerbig, C., Koch, F.-T., Smith, N.E., Thompson, R.L., Luijkx, I.T., White, E., Meesters, A., Ciais, P., Ganesan, A.L., Manning, A., Mischurow, M., Peters, W., Peylin, P., Tarniewicz, J., Rigby, M., Rödenbeck, C., Vermeulen, A., Walton, E.M., 2020. The regional European atmospheric transport inversion comparison, EUROCOM: first results on European-wide terrestrial carbon fluxes for the period 2006–2015. Atmos. Chem. Phys. 20, 12063–12091. https://doi.org/10.5194/acp-20-12063-2020.

Nevison, C.D., Weiss, R.F., Erickson III, D.J., 1995. Global oceanic emissions of nitrous oxide. J. Geophys. Res. 100 (C8), 15809–15820. https://doi.org/10.1029/95JC00684.

Patra, P.K., Takigawa, M., Watanabe, S., Chandra, N., Ishijima, K., Yamashita, Y., 2018. Improved chemical tracer simulation by MIROC4. 0-based atmospheric chemistry-transport model (MIROC4-ACTM). Sola 14, 91–96.

Pattey, E., Edwards, G.C., Desjardins, R.L., Pennock, D.J., Smith, W., Grant, B., MacPherson, J.I., 2007. Tools for quantifying N_2O emissions from agroecosystems. Agric. Forest Meteorol. 142, 103–119.

Pattey, E., Blackburn, L.G., Strachan, I.B., Desjardins, R., Dow, D., 2008. Spring thaw and growing season N_2O emissions from a field planted with edible peas and a cover crop. Can. J. Soil Sci. 88, 241–249.

Peyridieu, S., Chédin, A., Tanré, D., Capelle, V., Pierangelo, C., Lamquin, N., Armante, R., 2010. Saharan dust infrared optical depth and altitude retrieved from AIRS: a focus over North Atlantic – comparison to MODIS and CALIPSO. Atmos. Chem. Phys. 10, 1953–1967. https://doi.org/10.5194/acp-10-1953-2010.

Pison, I., Bousquet, P., Chevallier, F., Szopa, S., Hauglustaine, D., 2009. Multi-species inversion of CH_4, CO and H_2 emissions from surface measurements. Atmos. Chem. Phys. 9, 5281–5297. https://doi.org/10.5194/acp-9-5281-2009.

Pison, I., Berchet, A., Saunois, M., Bousquet, P., Broquet, G., Conil, S., Delmotte, M., Ganesan, A., Laurent, O., Martin, D., O'Doherty, S., Ramonet, M., Spain, T.G., Vermeulen, A., Yver Kwok, C., 2018. How a European network may help with estimating methane emissions on the French national scale. Atmos. Chem. Phys. 18, 3779–3798. https://doi.org/10.5194/acp-18-3779-2018.

Pisso, I., Sollum, E., Grythe, H., Kristiansen, N.I., Cassiani, M., Eckhardt, S., Arnold, D., Morton, D., Thompson, R.L., Groot Zwaaftink, C.D., Evangeliou, N., Sodemann, H., Haimberger, L., Henne, S., Brunner, D., Burkhart, J.F., Fouilloux, A., Brioude, J., Philipp, A., Seibert, P., Stohl, A., 2019. The Lagrangian particle dispersion model FLEXPART version 10.4. Geosci. Model Dev. 12, 4955–4997. https://doi.org/10.5194/gmd-12-4955-2019.

Prather, M.J., Hsu, J., DeLuca, N.M., Jackman, C.H., Oman, L.D., Douglass, A.R., Fleming, E.L., Strahan, S.E., Steenrod, S.D., Søvde, O.A., Isaksen, I.S.A., Froidevaux, L., Funke, B., 2015. Measuring and modeling the lifetime of Nitrous Oxide including its variability. J. Geophys. Res. 120, 5693–5705. https://doi.org/10.1002/2015JD023267.

Ravishankara, A., Daniel, J.S., Portmann, R.W., 2009. Nitrous oxide (N_2O): the dominant ozone-depleting substance emitted in the 21st century. Science 326, 123–125. https://doi.org/10.1126/science.1176985.

Ricaud, P., Attié, J.-L., Teyssedre, H., Amraoui, L.E., Peuch, V.-H., Matricardi, M., Schluessel, P., 2009. Equatorial total column of nitrous oxide as measured by IASI on MetOp-A: implications for transport processes. Atmos. Chem. Phys. 9, 3947–3956. https://doi.org/10.5194/acp-9-3947-2009.

Ricaud, P., Sič, B., El Amraoui, L., Attié, J.-L., Zbinden, R., Huszar, P., Szopa, S., Parmentier, J., Jaidan, N., Michou, M., Abida, R., Carminati, F., Hauglustaine, D., August, T., Warner, J., Imasu, R., Saitoh, N., Peuch, V.-H., 2014. Impact of the Asian monsoon anticyclone on the variability of mid-to-upper tropospheric methane above the Mediterranean Basin. Atmos. Chem. Phys. 14, 11427–11446. https://doi.org/10.5194/acp-14-11427-2014.

Rodgers, C.D., 2000. Inverse Methods for Atmospheric Sounding: Theory and Practice, Vol. 2. World Scientific Singapore.

Saito, R., Patra, P.K., Deutscher, N., Wunch, D., Ishijima, K., Sherlock, V., Blumenstock, T., Dohe, S., Griffith, D., Hase, F., Heikkinen, P., Kyrö, E., Macatangay, R., Mendonca, J., Messerschmidt, J., Morino, I., Notholt, J., Rettinger, M., Strong, K., Sussmann, R., Warneke, T., 2012. Technical Note: latitude-time variations of atmospheric column-average dry air mole fractions of CO_2, CH_4 and N_2O. Atmos. Chem. Phys. 12 (7767–7777), 2012. https://doi.org/10.5194/acp-12-7767-2012.

Saunders, R., Matricardi, M., Brunel, P., 1999. A Fast Radiative Transfer Model for Assimilation of Satellite Radiance Observations-RTTOV-5. European Centre for Medium-Range Weather Forecasts.

Shurpali, N., Rannik, Ü., Jokinen, S., Lind, S., Biasi, C., Mammarella, I., Peltola, O., Pihlatie, M., Hyvönen, N., Räty, M., Haapanala, S., Zahniser, M., Virkajärvi, P., Vesala, T., Martikainen, P.J., 2016. Neglecting diurnal variations leads to uncertainties in terrestrial nitrous oxide emissions. Sci. Rep. 6, 25739. https://doi.org/10.1038/srep25739.

Therond, O., Tichit, M., Tibi, A., Accatino, F., Biju-Duval, L., Bockstaller, C., Bohan, D., Bonaudo, T., Boval, M., Cahuzac, E., Casellas, E., Chauvel, B., Choler, P., Constantin, J., Cousin, I., Daroussin, J., David, M., Delacote, P., Derocles, S., de Sousa, L., Domingues, J.P., Dross, C., Duru, M., Eugène, M., Fontaine, C., Garcia, B., Geijzendorffer, I.R., Girardin, A., Graux, A.-I., Jouven, M., Langlois, B., Le Bas, C., Le Bissonnais, Y., Lelievre, V., Lifran, R., Maigne, E., Martin, G., Märtin, R., Martin-Laurent, F., Martinet, V., Mclaughlin, O., Meillet, A., Mignolet, C., Mouchet, M., Nozieres-Petit, M.-O., Ostermann, O.P., Paracchini, M.L., Pellerin, S., Peyraud, J.-L., Petit, S., Picaud, C., Plantureux, S., Poméon, T., Porcher, E., Puech, T., Puillet, L., Rambonilaza, T., Raynal, H., Resmond, R., Ripoche, D., Ruget, F., Rulleau, B., Rush, A., Salles, J.-M., Sauvant, D., Schott, C., Tardieu, L., 2017. Volet écosystèmes agricoles de l'Evaluation Française des Ecosystèmes et des Services Ecosystémiques. Rapport d'étude. INRA, France. https://doi.org/10.15454/prmv-wc85, 966.

Thompson, R.L., Chevallier, F., Crotwell, A.M., Dutton, G., Langenfelds, R.L., Prinn, R.G., Weiss, R.F., Tohjima, Y., Nakazawa, T., Krummel, P.B., Steele, L.P., Fraser, P., O'Doherty, S., Ishijima, K., Aoki, S., 2014. Nitrous oxide emissions 1999 to 2009 from a global atmospheric inversion. Atmos. Chem. Phys. 14, 1801–1817.

Thompson, R.L., Lassaletta, L., Patra, P.K., Wilson, C., Wells, K.C., Gressent, A., Koffi, E. N., Chipperfield, M.P., Winiwarter, W., Davidson, E.A., Tian, H., Canadell, J.G., 2019. Acceleration of global N_2O emissions seen from two decades of atmospheric inversion. Nat. Clim. Chang. 9 (12), 993–998.

Tian, H., Chen, G., Lu, C., Xu, X., Ren, W., Zhang, B., Banger, K., Tao, B., Pan, S., Liu, M., Zhang, C., Bruhwiler, L., Wofsy, S., 2015. Global methane and nitrous oxide emissions from terrestrial ecosystems due to multiple environmental changes. Ecosyst. Health Sustain. 1 (1), 1–20.

Tian, H., Xu, R., Canadell, J.G., Thompson, R.L., Winiwarter, W., Suntharalingam, P., Davidson, E.A., Ciais, P., Jackson, R.B., Janssens-Maenhout, G., Prather, M.J., Regnier, P., Pan, N., Pan, S., Peters, G.P., Shi, H., Tubiello, F.N., Zaehle, S., Zhou, F., Arneth, A., Battaglia, G., Berthet, S., Bopp, L., Bouwman, A.F., Buitenhuis, E.T., Chang, J., Chipperfield, M.P., Dangal, S.R.S., Dlugokencky, E., Elkins, J.W., Eyre, B. D., Fu, B., Hall, B., Ito, A., Joos, F., Krummel, P.B., Landolfi, A., Laruelle, G.G., Lauerwald, R., Li, W., Lienert, S., Maavara, T., MacLeod, M., Millet, D.B., Olin, S., Patra, P.K., Prinn, R.G., Raymond, P.A., Ruiz, D.J., van der Werf, G.R., Vuichard, N., Wang, J., Weiss, R.F., Wells, K.C., Wilson, C., Yang, J., Yao, Y., 2020. A comprehensive quantification of global nitrous oxide sources and sinks. Nature 586 (7828), 248–256.

Wagner-Riddle, C., Congreves, K.A., Abalos, D., Berg, A.A., Brown, S.E., Ambadan, J.T., Gao, X., Tenuta, M., 2017. Globally important nitrous oxide emissions from croplands induced by freeze-thaw cycles. Nat. Geosci. 10, 279–283. https://doi.org/10.1038/ngeo2907.

Wells, K.C., Millet, D.B., Bousserez, N., Henze, D.K., Griffis, T.J., Chaliyakunnel, S., Dlugokencky, E.J., Saikawa, E., Xiang, G., Prinn, R.G., O'Doherty, S., Young, D., Weiss, R.F., Dutton, G.S., Elkins, J.W., Krummel, P.B., Langenfelds, R., Steele, L.P., 2018. Top-down constraints on global N_2O emissions at optimal resolution: application of a new dimension reduction technique. Atmos. Chem. Phys. 18, 735–756. https://doi.org/10.5194/acp-18-735-2018.

Werner, C., Butterbach-Bahl, K., Haas, E., Hickler, T., Kiese, R., 2007. A global inventory of N_2O emissions from tropical rainforest soils using a detailed biogeochemical model. Glob. Biogeochem. Cycles 21. https://doi.org/10.1029/2006gb002909.

Xiong, X., Maddy, E.S., Barnet, C., Gambacorta, A., Patra, P.K., Sun, F., Goldberg, M., 2014. Retrieval of nitrous oxide from Atmospheric Infrared Sounder: characterization and validation. J. Geophys. Res. Atmos. 119, 9107–9122. https://doi.org/10.1002/2013JD021406.